Protolith age, and timing of burial and exhumation of the UHP Chasteiran Unit (Dora-Maira Massif, Western Alps), constrained by zircon, garnet and rutile petrochronology

Paola Manzotti, Leo J Millonig, Axel Gerdes, Martin J Whitehouse, Heejin Jeon, Marc Poujol, Michel Ballèvre

LITHOS 496–497 (2025) 107951

Contents lists available at ScienceDirect

LITHOS

journal homepage: www.elsevier.com/locate/lithos

Protolith age, and timing of burial and exhumation of the *UHP* Chasteiran Unit (Dora-Maira Massif, Western Alps), constrained by zircon, garnet and rutile petrochronology

Paola Manzotti [a,*], Leo J. Millonig [b,c], Axel Gerdes [b,c], Martin J. Whitehouse [d], Heejin Jeon [d], Marc Poujol [e], Michel Ballèvre [e]

[a] *Department of Geological Sciences, Stockholm University, 106 91 Stockholm, Sweden*
[b] *Department of Geosciences, Goethe-University Frankfurt, Altenhöferallee 1, 60438 Frankfurt am Main, Germany*
[c] *Frankfurt Isotope and Element Research Center (FIERCE), Goethe-University Frankfurt, Germany*
[d] *Swedish Museum of Natural History, Stockholm 104 05, Sweden*
[e] *Geosciences Rennes-UMR 6118, University of Rennes, F35000 Rennes, France*

A R T I C L E I N F O

Keywords:
Coesite
Dora-Maira
Chasteiran
Continental subduction
U-Pb geochronology

A B S T R A C T

The Chasteiran Unit in the northern Dora-Maira Massif reached ultra-high-pressure conditions in the chloritoid-coesite stability field. The chemical and isotopic behaviours of zircon, garnet, and rutile from a metapelite were explored to reconstruct the metamorphic evolution of this Unit.

Zircon crystals display detrital cores and thin (< 5 μm) metamorphic rims which cannot be dated. The dominant zircon population consists of Late Neoproterozoic (~600 Ma) magmatic grains whereas the youngest zircon cluster is Ordovician in age (~470 Ma).

Garnet records three main growth stages: initial growth during a prograde pressure and temperature increase in the quartz stability field (2.5–2.7 GPa at 470–500 °C, inner core – stage 1), peak growth in the coesite stability field (2.7–2.8 GPa at 510–530 °C, outer core – stage 2), and final growth of the garnet rim between 2.3 GPa 520 °C and 1.5 GPa 510 °C (stage 3), contemporaneously with lawsonite consumption coupled with fluid production.

LA-ICP-MS U-Pb dating of garnet indicates two distinct stages of growth for garnet cores and rims at ~61 Ma and ~43 Ma, respectively. The time interval separating the growth of garnet cores and rims is consistent with our thermodynamic modelling, which indicates the absence of garnet growth during the initial stage of exhumation, between 2.7. GPa and 2.3 GPa.

Rutile is found both as inclusions in garnet and in the matrix. Rare inclusions of jadeite and Si-rich muscovite also indicate stability of rutile during burial at a minimum pressure of 2.0 GPa. Inclusions of rutile in garnet are commonly surrounded by fractures and some crystals display ilmenite exsolution lamellae, suggesting that despite their mode of occurrence, they might have behaved as an open system during retrograde metamorphism. Rutile consumption took place during exhumation, as suggested by the increase in Ti content in garnet and muscovite rims and thermodynamic modelling. Rutile in the matrix is partially replaced by ilmenite corona, which developed at $P < 1.5$ GPa, after garnet growth. SIMS U-Pb dating of rutile, irrespective of its petrographic mode of occurrence, yields a date of ~37 Ma.

Our geochronological data suggest a different timing of burial and exhumation for the northern and southern Dora-Maira Massif and imply that the peak ultra-high-pressure episode in the northern Dora-Maira Massif is older than the peak eclogite-facies in the overlying oceanic units. Therefore, different extensional allochthons derived from the Briançonnais hyperextended palaeomargin may have been buried and/or detached from the downgoing slab at different times.

* Corresponding author.
E-mail address: paola.manzotti@geo.su.se (P. Manzotti).

https://doi.org/10.1016/j.lithos.2025.107951
Received 13 October 2024; Received in revised form 30 December 2024; Accepted 17 January 2025
Available online 21 January 2025

1. Introduction

An orogenic cycle consists of a continuous succession of geologic events, involving changes in pressure (i.e. burial and exhumation), temperature (i.e. heating and cooling), and fluid production and consumption in partially closed to open systems. These changes in intensive (*P*, *T*) and extensive (H_2O content) variables are recorded by the complex adjustment of mineral assemblages and the major and trace element compositions of main and accessory phases. Linking an isotopic date to a specific segment of an orogenic cycle is therefore a major challenge.

Anchoring dates to *P*–*T* paths of ultra-high-pressure (*UHP*) metamorphic rocks represents an additional difficulty, because their *P*–*T* paths commonly display (i) a very steep slope with an increase in *P* over a short *T* range during burial, and (ii) nearly isothermal decompression following peak *P* (e.g., McClelland and Lapen, 2013), potentially acquired over very short time (*t*) scales (e.g., Rubatto and Hermann, 2001). Two main approaches need to be combined to obtain a *P*–*T*–*t* path. The first one is based on equilibrium thermodynamics which allows for the assignment of mineral assemblages and compositions to specific *P*–*T* conditions (e.g., Powell and Holland, 2010); the second one is based on cutting-edge isotopic dating techniques and on the understanding of the potential closure mechanism for the investigated isotopic system (e.g., Nemchin et al., 2013). Moreover, significant advances in analytical techniques over the last few decades allowed expanding the arsenal of geochronometers and dating smaller sample size with greater precision (e.g., Baxter et al., 2017).

In this study, we will provide new age constraints for the burial and exhumation of the recently discovered Chasteiran Unit in the northern Dora-Maira Massif in the Western Alps (Manzotti et al., 2022; Nosenzo et al., 2024). The investigated garnet-chloritoid micaschists are of normal pelitic composition and very different from the world-wide known whiteschists (pyrope-kyanite schists resulting from Mg-metasomatism) from the Brossasco-Isasca Unit in the southern Dora-Maira Massif (e.g., Chopin, 1984; Ferrando et al., 2009). This study highlights the diversity of *UHP* metamorphism in the Western Alps and discusses its consequences for the geodynamic processes involved in their genesis.

2. Geological background

2.1. Tectonic architecture of the northern Dora-Maira Massif

The studied rocks have been sampled in the Chasteiran Unit (Fig. 1), in the northern part of the Dora-Maira Massif (Ballèvre et al., 2020; Michard et al., 2022). The latter is a window below the eclogite-facies, oceanic units derived from the Piemonte-Liguria Ocean. The Dora-Maira Massif consists of a stack of subducted continental-units, belonging to the easternmost part of the Briançonnais microcontinent. A description of all tectonic units in the northern Dora-Maira Massif has recently been provided by Nosenzo et al. (2024) and will not be detailed here. However, for the purpose of this study, the following points are relevant.

The lowest unit, namely the Pinerolo Unit, consists of metaconglomerates, metasandstones and minor coal (now graphite) layers deposited under various sedimentary environments (from lacustrine to fluviatile) and characterized by the abundance of graphite, giving them a characteristic grey to black colour (Nosenzo et al., 2024). Their age is assumed to be Carboniferous, consistent with the detrital zircon geochronology of these metasediments (Manzotti et al., 2016).

The Chasteiran Unit, which is the subject of this study, is located on top of the Pinerolo Unit and consists of chloritoid micaschist, with sparse garnet crystals. These micaschists may also contain graphite. The Chasteiran Unit differs from other units in the northern Dora-Maira Massif in that it retains evidence of *UHP* metamorphism, as recorded by coesite inclusions in garnet, and in the chemical composition of garnet (Manzotti et al., 2022). No geochronological data are available on the Chasteiran Unit so far.

On top of the Chasteiran Unit, a large thrust sheet, the Muret Unit, displays a polycyclic basement, with relicts of Ordovician granodioritic intrusions (Bussy and Cadoppi, 1996; Nosenzo et al., 2022) predating an episode of Barrovian metamorphism dated at ~325 Ma (Nosenzo et al., 2022). Preservation of the pre-Alpine assemblages is due to the limited

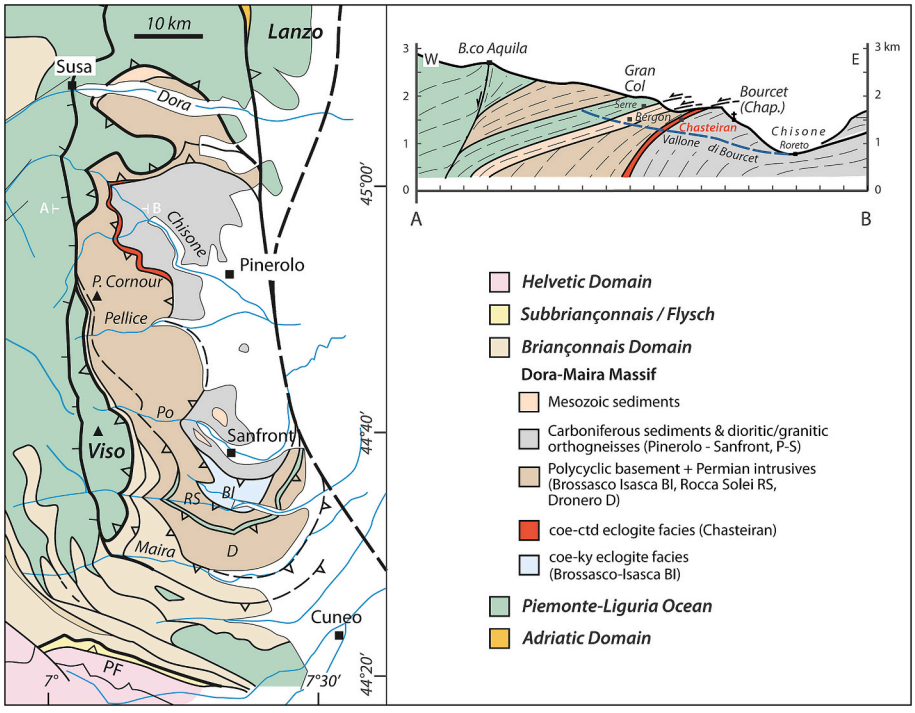

Fig. 1. Simplified tectonic map of the SW Alps, showing the internal architecture of the Dora-Maira Massif (modified after Ballèvre et al., 2020). PF Penninic Front. The position of the cross-section on the map is indicated by the letters AB (modified after Nosenzo et al., 2024).

involvement of fluids during the Alpine orogeny (Nosenzo et al., 2023). The base of the Muret Unit is defined by a thin sheet of mylonitic augen orthogneisses, which have also provided Ordovician ages (Nosenzo et al., 2024). During the Alpine orogeny, the Muret Unit experienced an eclogite-facies metamorphism (21–22 kbar, 530–560 °C; Nosenzo et al., 2023).

On top of the Muret Unit, the Serre Unit displays Permian orthogneiss dated at ~270 Ma (Nosenzo et al., 2024) and garnet-chloritoid micaschist, on top of which there are thinned and boudinaged remnants of a Mesozoic cover, the most characteristic lithology being marbles and dolostones of presumed Triassic age.

2.2. *P–T evolution of the Chasteiran Unit*

The Chasteiran Unit reached *UHP* metamorphic conditions in the chloritoid stability field (Manzotti et al., 2022). Garnet displays a record of growth with three main stages: a prograde increase in *P* and *T* (2.5–2.7 GPa 470–500 °C; stage 1) in the quartz stability field, then the peak in the coesite stability field (2.7–2.8 GPa 510–530 °C; stage 2), and a nearly isothermal decompression back into the quartz stability field (down to 1.5 GPa 500–515 °C; stage 3). Coesite crystals occur in the garnet outer cores and record a "short", transitory, stage representing the culmination of the burial of the Chasteiran Unit. Ductile deformation is recorded during the entire evolution of the rock. However, the main regional, composite, foliation, marked by chloritoid and white mica developed during stage 3 in the rutile stability field, and was subsequently overprinted by chlorite–ilmenite after garnet growth had ceased (stage 4).

3. Methods

3.1. *Petrography and mineral chemistry*

Hereafter, figures, tables, and appendices given in the Supporting Information are referred to as 'Fig. S' and 'Table S', and 'Appendix S'. In order to reconstruct a timeline for the metamorphic evolution of the Chasteiran Unit, we studied rutile and garnet in six different polished thin sections (Figs. S1-S6) cut from a garnet-chloritoid micaschist sample (sample CH11, Lat/Long coordinates 44° 59′ 21.75″ N–7° 06′ 29.03″ E) which was previously used for determining the *P–T* evolution of this Unit (Manzotti et al., 2022). The size, abundance and spatial distribution of garnet and rutile crystals (Figs. S7-S9, Table S1, and Appendix S1) were investigated by optical microscopy and image analysis using the software ImageJ (open-source; Rasband, 1997). Their chemistry and texture were studied by backscattered electron (BSE) imaging and electron microprobe analysis (EMPA). BSE images were obtained using a scanning electron microscope equipped with an energy dispersive spectrometer (SEM-EDS FEI Quanta FEG 650) at the Swedish Museum of Natural History. Point analyses and chemical maps were performed using an electron microprobe at the Institute of Earth Science in Lausanne, Switzerland (see Table S2 for detail on analytical conditions). Mineral inclusions in rutile were identified by Raman microspectroscopy at the Institute of Earth Sciences in Lausanne, Switzerland and details on this analytical method are given in Appendix S2. Mineral abbreviations are those used by THERMOCALC (Holland and Powell, 1998, Table S3). A list of other symbols adopted in this study are given in Table S3. Muscovite is used hereafter for all potassic white micas, whatever the Si content. Representative chemical analyses of selected minerals are given in Tables S4, S5, and S6.

3.2. *Thermodynamic modelling*

Compositional and modal isopleths were calculated for the *P–T* pseudosections published in Manzotti et al. (2022), with the aim of understanding the growth and consumption history of garnet in relation to other minerals. New phase diagrams were also calculated in the *P–T* range 0.5–1.5 GPa 300–400 °C and 0.5–1.5 GPa 400–600 °C, in order to explore the early stage of the burial of the Chasteiran Unit and the replacement of rutile by ilmenite during exhumation, respectively. Table S7 reports the phases considered in the calculations and the activity-composition models. Details on the bulk rock compositions used for these calculations are given in Appendices S3, S4 and Table S8.

3.3. *Geochronology*

In this study, the following strategy has been used for U-Pb geochronology. Because phosphates (monazite, xenotime, apatite) and REE-rich epidote (allanite) have not been found in the studied micaschist, potential targets for isotopic measurements are zircon, garnet and rutile. Garnet is a primary target, because its growth can be closely tied to the *P–T* history. Given its small modal proportion, its tiny size and its zoned character, it is not suitable for separating different fractions (core, rim) and using them for constructing Lu-Hf or Sm-Nd isochrons with the ID-TIMS technique (Baxter et al., 2017). However, a LA-ICP-MS study may prove useful, considering the recent advances for analysing garnet with a very low amount of U (Millonig et al., 2020). Rutile is an obvious candidate for dating the *UHP* metamorphism, because it is, like garnet, considered as a stable mineral at peak *UHP* conditions. With respect to garnet, however, the timing of growth and subsequent history of rutile is much less understood, and this will require an in-depth investigation of its chemical behaviour along the *P–T* path. In addition, because the rutile grains are small and their U content is very low, we have chosen to study them using the SIMS technique. Finally, zircon may seem a promising target, although previous experience in similar lithologies has shown that most zircon grains are detrital (e.g., Manzotti et al., 2015, 2016; Nosenzo et al., 2022), and only display very thin metamorphic overgrowths, generally inaccessible to the laser spot. Therefore, zircon U-Pb studies are not expected to date the Alpine metamorphic history, but may be used (i) to constrain the protolith age of the micaschist i.e. the sedimentation age, and (ii) to understand the effect of microinclusions when dating garnet.

3.3.1. *Garnet U-Pb dating by LA-ICPMS (FIERCE)*

For garnet and rutile dating we use the same polished thin sections cut from sample CH11 previously investigated for petrography, mineral chemistry, and thermodynamic modelling.

LA-ICPMS U–Th–Pb isotope analysis were conducted at FIERCE (Frankfurt Isotope & Element Research Center), Goethe University Frankfurt, Germany, using a RESOLution 193 nm ArF excimer laser coupled to a Neptune Plus multi-collector ICPMS. The method has been modified after Beranoaguirre et al. (2022). Detailed U-Pb data and acquisition parameters are given in the Supplementary file Table S9 and Appendix S1 (i.e. U-Pb data and metadata tables).

The signal was tuned for maximum sensitivity, low oxide formation (UO/U $\leq$ 0.3 %), and low element fraction (e.g. Th/U ~ 1), by line-ablation of the soda–lime glass NIST SRM 612 (Jochum et al., 2011) at 50 μm spot size, 6 Hz, ca. 3.5 J/cm^2 fluence, and 3 μm/s line speed. The sensitivity (see Schaltegger et al., 2015) was 1.69 %. The U-Th-Pb data was collected during 20 s of background, and 20 s of ablation in static mode, measuring ^{206}Pb and ^{207}Pb with the secondary electron multipliers (SEMs), ^{238}U with a compact discrete dynode SEM, and ^{232}Th on a Faraday cup with a 10^{13} Ω amplifier. NIST SRM 614 was used as the primary reference material to correct for ^{207}Pb/^{206}Pb mass bias, inter-element fractionation and instrumental drift (^{206}Pb/^{238}U). To determine the matrix-dependent offset in Pb/U fractionation between the NIST SRM 614 glass and garnet, we used demantoid garnet crystals (n = 4) from the Green Dragon Mine, Namibia, demantoid garnet crystals (n = 5) from Antetezambato, Madagascar, and andradite-grossular from Balochistan. In this analytical session, no matrix-dependent offset between NIST SRM 614 and the garnet reference materials was observed. However, NIST SRM 614 has been ablated with 75 μm spots, and garnet analyses were conducted with 108 μm spots. This difference in spot size

compensated the difference in Pb/U fractionation for this particular analytical session. The U-Pb date of 132.6 ± 2.6 Ma (MSWD = 0.8) for the Green Dragon Mine demantoids is within uncertainty of U-Pb and $^{40}Ar/^{39}Ar$ dates of 132.3 ± 1.9 Ma and 130.8 ± 1.0 Ma, respectively, obtained from the adjacent Erongo subvolcanic center (Wigand et al., 2004), responsible for the formation of the demantoid crystals. The U-Pb date of 18.24 ± 0.41 Ma (MSWD = 1.08) for the demantoids from Antetezambato is within uncertainty of apatite and titanite U-Pb dates of 18.86 ± 1.03 Ma and 17.80 ± 1.29 Ma, respectively, obtained from the lamprophyre that caused the formation of the demantoid crystals (FIERCE, unpublished data). The U-Pb date of 43.02 ± 2.20 Ma (MSWD = 0.91) for the U-poor rim (U_{avg} = 0.1 μg/g) of the Balochistan andradite-grossular is similar to a U-Pb date of 45.31 ± 0.46 Ma (ID-TIMS U-Pb FIERCE, unpublished data), obtained from the U-rich core (U ~ 15 μg/g) of the same crystal.

Raw data were corrected offline using an in-house VBA spreadsheet programme (Gerdes and Zeh, 2006; Gerdes and Zeh, 2009). Following background and interferences corrections, outliers (±2σ) were rejected based on the time-resolved $^{207}Pb/^{206}Pb$ and $^{206}Pb/^{238}U$ ratios. Spikes in the U and Pb signals, indicative of ablated inclusions, were rejected during data processing. Moreover, analyses that were continuously affected by inclusions, as observed in the time-resolved signal and characterized by elevated U-contents, were rejected from age calculations and are marked by italic fonts in the Appendix S1. Uncertainties (2σ) for each isotopic ratio are the quadratic addition of the within-run precision, counting statistic uncertainties of each isotope, and the excess of scatter and variance (Horstwood et al., 2016). Data are displayed in Tera-Wasserburg plots (Tera and Wasserburg, 1972) and the ages were calculated from the lower intercepts with the Concordia curve using the same algorithms as Isoplot 4.15 (Ludwig, 2003). The uncertainties given for each date (e.g., Green Dragon Mine demantoid, Namibia:132.6 ± 1.1 / 2.6 Ma) reflect the within-run precision of the particular measuring sequence (first uncertainty) and the long-term reproducibility of the method (second uncertainty) (cf. Horstwood et al., 2016). For the data interpretation and discussion, only the second uncertainties are considered.

3.3.2. Rutile U-Pb dating by SIMS (NRM)

The polished thin sections were cut and cast into epoxy disks. Rutile U-Pb dating was performed using a CAMECA IMS1280 ion microprobe (NordSIMS laboratory; Swedish Museum of Natural History, Stockholm). The analytical conditions are similar than those for zircon U-Pb analysis given in Whitehouse et al. (1999), with a few differences for rutile. Oregon Physics H201 RF Plasma source generated an O_2^- Gaussian primary beam of ca. 5 nA with an impact energy of 23 kV, and was rastered over 5 × 5 μm (spot size of <15 μm) during the analysis. Oxygen flooding was not employed. To minimize surface contamination and remove the Au coating, a 25 μm-rastered area was pre-sputtered for 80 s for each area analysed, followed by automated centring of the secondary ions onto the ion optical axis (using the matrix signal, $^{48}Ti_2^{16}O_4$), and then data acquisition with a mass resolution ca. 6000. Field of view of ca. 12 μm was achieved by closing the field aperture to 2000 μm without using DTOS (dynamic transfer operating system), and with a field magnification of ×160. This setup ensures that only signals from the central 12 μm area of the sputtered surface pass through the mass spectrometre. Data were processed using in-house SIMS data reduction spreadsheets and the Excel add-in Isoplot (Ludwig, 2008). Primary standard R10 (Luvizotto et al., 2009) was used to calibrate U-Pb, with a Pb/U-UO_2/U scheme: external precision of the U-Pb calibration is 1.4–2.1 % (1 sd). Secondary standard R13 were measured as unknowns and yielded the $^{206}Pb/^{238}U$ weighted mean age of 515 ± 38 Ma (2σ; n = 20; MSWD 0.06), which agree well with the published SIMS $^{206}Pb/^{238}U$ age of 504 ± 4 Ma (Schmitt and Zack, 2012). The relative error on single spot analyses is quoted as 2σ.

3.3.3. Zircon U-Pb dating by LA-ICPMS (GeOHeLiS)

Zircon grains from a garnet-chloritoid micaschist sample (named CH43, Lat/Long coordinates 44° 59′ 21.75″ N–7° 06′ 29.03″ E) collected in the same outcrop as sample CH11 were studied in order to assess the maximum age of deposition of the meta-sediments of the Chasteiran Unit. About 2 dm^3 of rock material was crushed and milled with a Resch PM400 tungsten steel mortar at Stockholm University. Zircon grains were separated from the light mineral fraction with a Wilfley Table. Zircon crystals were handpicked and mounted on a one-inch epoxy resin puck, subsequently polished to expose the equatorial section of the crystals.

Zircon grains were analysed by LA-ICP-MS with an ESI NWR193UC Excimer laser coupled to an Agilent quadrupole 7700× ICP-MS at the GeOHeLiS analytical platform (University of Rennes, France). Details on sample preparation, operating conditions for the LA-ICP-MS analyses and data processing are given in Table S10. Concordia ages were calculated with IsoplotR (Vermeesch, 2018). Detrital ages were plotted as Kernel density diagrams generated with the program DensityPlotter (Vermeesch, 2012). Single spot analyses are given as $^{207}Pb/^{206}Pb$ dates for results ≥1000 Ma and $^{206}Pb/^{238}U$ dates for results <1000 Ma (assessed on $^{206}Pb/^{238}U$). The relative error is quoted as 2σ, and concordia ages are given with 95 % confidence level. Mean squared weighted deviations (MSWD) are given for concordance plus equivalence. Concordance % was calculated as:

$$\left(\text{date}^{206}Pb/^{238}U/\text{date}^{207}Pb/^{235}U\right)^{*} 100 \left(\text{if date}^{206}Pb/^{238}U < 1000\ \text{Ma}\right)$$

or

$$\left(\text{date}^{207}Pb/^{235}U/\text{date}^{207}Pb/^{206}Pb\right)^{*} 100 \left(\text{if date}^{206}Pb/^{238}U > 1000\ \text{Ma}\right)$$

The data were filtered for discordance using a threshold of discordance of ±10 %, which is considered as most appropriate for identifying the major age peaks (see discussion in Ewing et al., 2023). For our purpose, the relative proportions of different age peaks or the age of a specific age components in the detrital spectra are of secondary importance. In addition, the ±10 % threshold of discordance was used in previous detrital zircon studies in the Internal Crystalline Massif (Dora-Maira and Gran Paradiso Massifs; Manzotti et al., 2015 and Manzotti et al., 2016; Nosenzo et al., 2024) allowing a comparison between the different detrital datasets. The maximum age of deposition from detrital zircon U-Pb data was determined calculating the youngest age population on the basis of the weighted mean of at least three analyses that agree at 2σ (Dickinson and Gehrels, 2009). The detrital zircon U-Pb ages dataset is given in Appendix S1.

4. Results

4.1. Garnet texture and chemistry (sample CH11)

We refer to Manzotti et al. (2022) for a complete petrographic and microstructural description of the garnet-chloritoid micaschist from the Chasteiran Unit, while in this study we mainly focus on the chemical and textural characters of garnet and rutile.

The six thin sections cut from sample CH11 contain a few idioblastic garnet porphyroblasts (up to 5 mm in size; Figs. S1-S6), which occupy on average 6 vol% (Table S1 and Fig. S7). Garnet is optically and chemically zoned (Fig. 2) and shows large (up to 4.5 mm-thick) colourless cores and thin (up to 500 μm-thick) light pink rims. The latter may locally show porosity (Figs. 2c and S8).

Despite the fact that the growth of garnet cores is a continuous process, as shown by the smooth and gentle changes in its composition, it may be useful to distinguish an inner and an outer garnet core for describing the *P–T* evolution during garnet growth. This may be done using the following criteria (Manzotti et al., 2022): (i) the presence of quartz (inner core) or coesite (outer core); and (ii) in the lack of SiO_2

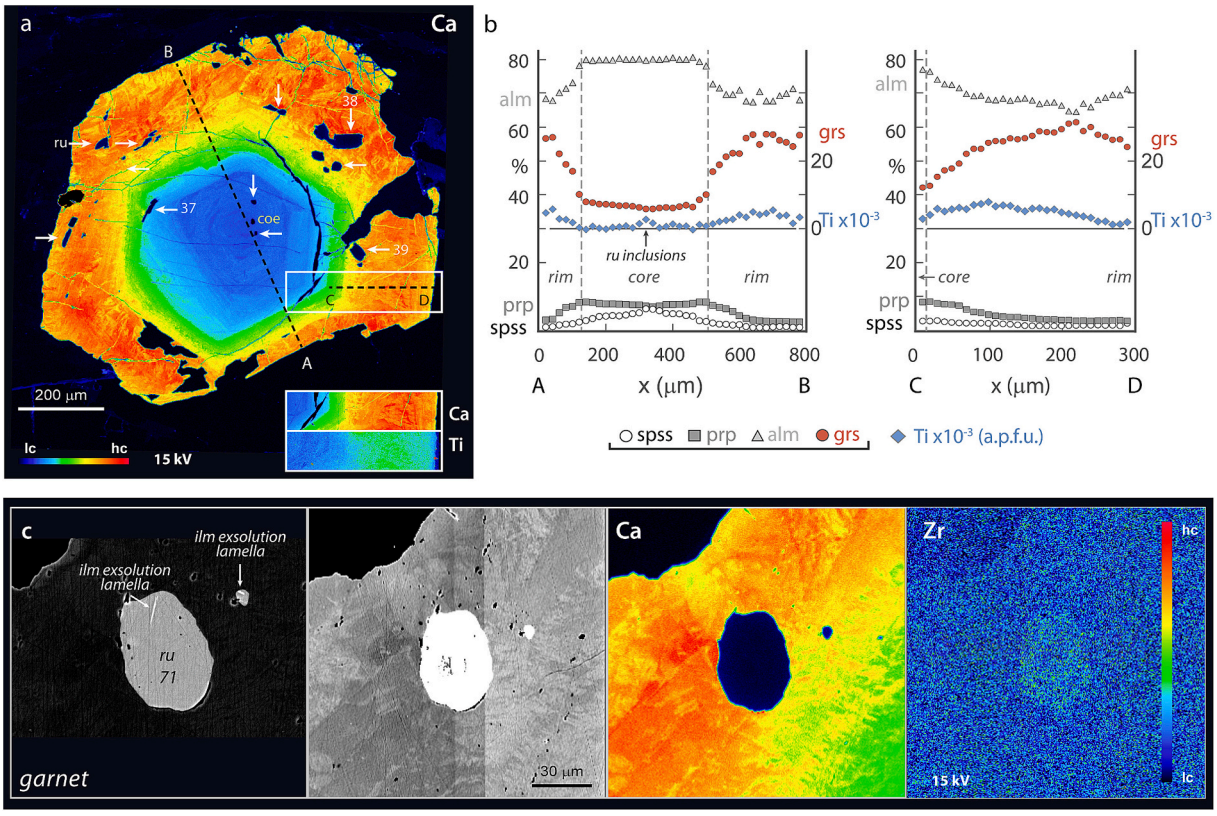

Fig. 2. (a) X-ray maps of Ca and Ti (inset in right bottom corner) of a garnet porphyroblast displaying rutile inclusions in the core and rim (white arrows). Coesite is found in the core. Numbers refer to the analysed rutile crystals (see Fig. S8) (b) Compositional profiles of garnet. References for Ti and grossular data are shown on the right y-axis. The boundaries between core and rim is denoted by vertical grey dashed lines. The position of the profiles (black dashed lines A–B and C-D) is reported in Fig. 2a. Note also drop in Ti concentration around rutile inclusion (profile A–B) in garnet core and the continuous increase in Ti with increasing grossular content in the garnet rim (profiles A–B and C-D). (c) BSE and X-ray maps of rutile grains included in garnet rim (see Fig. S10 for BSE image of the entire garnet crystal). The first two images are BSE images acquired with different brightness/contrast degrees. Rutile grains display exsolution lamellae whereas garnet rims show Ca patchy zoning and some pores.

polymorphs, the garnet chemistry. However, we should be aware of the following points. (1) A thin section cut effect is always present. All garnet porphyroblasts are not necessarily cut through their "true" geometrical centre and this is unavoidable during the thin section processing. (2) Even if all grains are cut through their "true" centres, they will not necessarily display the same chemical composition if nucleation has taken place over a *T* interval. In other words, garnet cores will display the same chemistry only if all nuclei have been formed exactly at the same *P*–*T* conditions (disregarding the potential effect of the local bulk composition; i.e. of an equilibrium volume at a much small scale than the one of the thin section). (3) Some relaxation of the Mn bell-shaped profiles may have taken place and this adds a further complexity to the definition of the garnet inner and outer core. For practical purposes, the following criterion can be applied: garnet inner core is defined by a higher spessartine content with respect to the pyrope content; garnet outer core by a lower spessartine content than the pyrope content. If we use this criterion, the garnet core from Fig. 2 is an outer core because it shows a lower spessartine content than pyrope and it displays coesite inclusions. By contrast, the garnet porphyroblasts shown on Fig. 5a and detailed in Manzotti et al. (2022) displays both inner and outer core.

Taking this definition into account, the chemical evolution during garnet growth may be described as follows. Spessartine (from 12 to 3 mol%) decreases continuously from the centre of the inner cores to the edge of the outer cores, while almandine (from 75 to 80 mol%) and pyrope (from 6 to 9 mol%) increase progressively. The grossular (gr ~ 5–6 mol%) and Ti contents (Ti <0.001 a.p.f.u.) remain approximately constant over the inner cores and most of the outer cores and increase significantly at the outermost cores (gr up to ~9 mol%). Garnet rims show a sharp decrease in almandine (from 80 to 67 mol%), spessartine (from 3 to 1 mol%) and pyrope (from 9 to 3 mol%, Fig. 2b). Grossular strongly increases (from 9 to 29–30 mol%; Fig. 2) and then slightly decreases (from 29 to 30 to 22 mol%). Ti content increases in garnet rims (from 0.002 to 0.0079 a.p.f.u.) and displays a positive correlation with the highest grossular content (Fig. 2). Major element zoning maps reveal that some garnet rims show a small-scale, low amplitude patchy variation for grossular content (Fig. 2a and c).

The interface between garnet outer cores and rims is regularly shaped with rare and small embayments and does not correspond to an optical discontinuity (beyond the colour change).

Garnet inner cores contain inclusions of chloritoid, rutile, quartz, tourmaline, and polymineralic aggregates of paragonite + minor epidote ± muscovite (the latter interpreted as pseudomorphs after lawsonite, Manzotti et al., 2022). Inclusions of coesite, chloritoid, graphite, rutile and polycrystalline aggregates of quartz are observed in the garnet outer cores. Garnet rims display rare monomineralic inclusions of rutile, quartz, tourmaline, and epidote.

Garnet crystals are wrapped by the main matrix foliation and are preferentially found in high-Si muscovite layers. Matrix muscovite (Fig. 3) shows chemical zoning with decreasing Si content from core (Si = 3.40–3.47 a.p.f.u.) to rim (Si = 3.30–3.37 a.p.f.u.). The chemical analyses of muscovite rims plot above the ideal celadonite substitution (Fig. 3a), suggesting the presence of some Fe^{3+}. The Ti content of muscovite is low (< 0.28 wt%) and negatively correlated with the Si content (from 0.0063 in the core to 0.0141 a.p.f.u. in the rim; Figs. 3b-c).

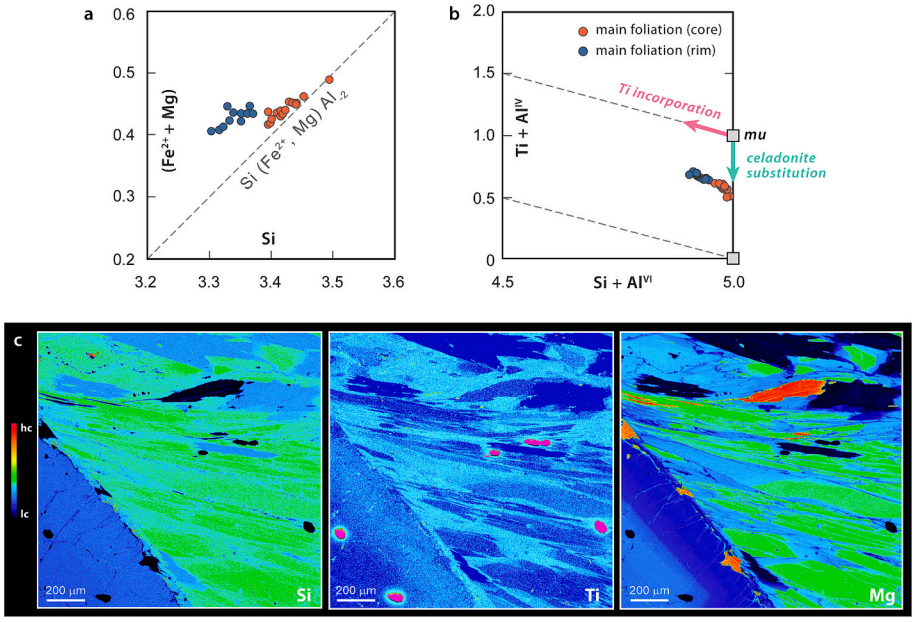

Fig. 3. Potassic white mica composition plotted in the Si vs. Ti (a.p.f.u.) diagram (a) and in the Si + Al^{VI} vs. Ti + Al^{IV} diagram (b). By convention, muscovite Al^{IV} is the amount needed to fill the tetrahedral sites. (c-e) X-ray maps of Si, Ti, and Mg of white mica marking the main composite foliation.

4.2. Rutile texture and chemistry (sample CH11)

Sample CH11 contains numerous rutile grains, which occupy on average 0.62 vol% (Table S1, Fig. S7). *Rutile included in garnet* (0.05 vol %) occurs as prismatic (30–170 µm long) or sub-rounded (30–70 µm in size) grains (Figs. 4, S8, S13-S15) with slightly irregular and curved borders and embayments (e.g., rutile 56 in Fig. S15). A few prismatic crystals located in the garnet rims are oriented parallel to the main matrix foliation (e.g., rutile 5 in Fig. 4). Rutile frequently displays internal cracks and the host garnet commonly shows open or chlorite-filled fractures around rutile inclusions (Appendix S1 and Figs. 4, S13-S15).

Matrix rutile (0.57 vol%) is found in the muscovite and chloritoid layers. Crystals (up to 300 µm in size) are generally elongated parallel to the main foliation and show corroded rims and embayments. In the muscovite layers, rutile is only partially replaced by thin ilmenite ±zircon coronas (Fig. 4c-d and Fig. S9). Tiny zircon grains also occur in the matrix in the proximity of rutile partially replaced by ilmenite (Fig. S9). Conversely, in the chloritoid layers, the replacement of rutile by ilmenite is commonly complete and rutile is rarely preserved as sub-rounded grains surrounded by thick ilmenite overgrowths (Figs. S1-S6).

Monomineralic inclusions of prismatic jadeite (Fig. 4e), Si-rich muscovite (Si = 3.47 a.p.f.u.; Fig. 4b and Table S5) and zircon (Figs. S8 and S9) in rutile are rare and tiny (from 3 to 10 µm in size) and were mainly found in rutile included in garnet cores and surrounded by fractures. Note that jadeite is not identified in the matrix. Muscovite included in rutile and the cores of matrix muscovite display similar chemical compositions (for a comparison, see Fig. S5 in Manzotti et al., 2022). Ilmenite exsolution lamellae displaying rational crystallographic orientation relationships with the rutile host are frequently observed in both rutile in the matrix and included in garnet (Figs. 4c, S8 and S9, Appendix S1).

Both rutile in the matrix and included in garnet contain variable amounts of minor and trace elements (Table S6), including V (0.001–0.004 a.p.f.u.), Cr (<0.001 a.p.f.u), Nb (0.003–0.005 a.p.f.u) and Y (<0.001 a.p.f.u). Crystals are slightly zoned with a decrease in V from core to rim. Zr content is below EMP detection limits (see Table S2). For this reason, even if the equilibrium mineral assemblage of quartz/coesite + rutile is present within the garnet crystals, the Zr-in-rutile thermometry was not applied to the investigated sample (e.g., Zack et al., 2004). Ilmenite contains only minor Mn (0.014 a.p.f.u.); structural formula calculations did not detect Fe^{3+}.

4.3. Thermodynamic modelling

Thermodynamic modelling (Figs. 5–7) was applied to investigate the behaviour of several phases (e.g., garnet, rutile, jadeite, glaucophane, chloritoid, muscovite, and H_2O) along the *P–T* path of increasing *P* (i.e. burial) and decreasing *P* (i.e. exhumation) reconstructed by Manzotti et al. (2022).

4.3.1. Burial of the Chasteiran Unit

A pseudosection was calculated in the system MnNCKFMASHTO in the *P–T* range 0.5–1.5 GPa and 300–400 °C, considering excess H_2O and using the bulk composition obtained by XRF (Manzotti et al., 2022). This calculation aims to assess when rutile grew in the studied sample.

Thermodynamic modelling shows that rutile coexisting with titanite is already present in minor modal amount (~0.1 vol%, Fig. 5b) at ~0.5 GPa 300–400 °C. Its abundance rapidly increases from 0.2 to 0.55 vol% between 0.95 and 1.3 GPa at 300–400 °C, due to titanite breakdown, which provides Ti for rutile and Ca for lawsonite. In the investigated *P–T* space, the Si content of muscovite varies between 3.10 a.p.f.u. and 3.37 a.p.f.u. The isomodes of this mineral are *P*-dependent with a positive slope: along an up-pressure and up-temperature *P–T* path, the modal amount of muscovite remains constant and high (~ 41–42 vol%).

Previous calculations were performed in the *P–T* range 1.5–3.5 GPa / 400–600 °C for the same bulk composition, modified after fractionation of the inner garnet cores (Manzotti et al., 2022). They showed that garnet inner and outer cores display a continuous record of growth, characterized by an increase in *P* and *T* (2.5–2.7 GPa 470–500 °C) in the quartz stability field and then a peak in the coesite stability field (2.7–2.8 GPa 510–530 °C; Fig. 5c). Along this prograde *P–T* path, both Si-rich muscovite (Si = 3.45–3.47 a.p.f.u.) and jadeite are present, with the latter being stable at a minimum *P* of 2.0 GPa (Fig. 5c). Along this final prograde *P–T* path, there is an overall increase in the modal amount of rutile (+0.02 vol%), jadeite (+0.22 vol%), H_2O (+0.50 vol%), muscovite (+0.66 vol%), and garnet (+3.00 vol%) and a total decrease in the modal abundance of glaucophane (−4.28 vol%), chloritoid

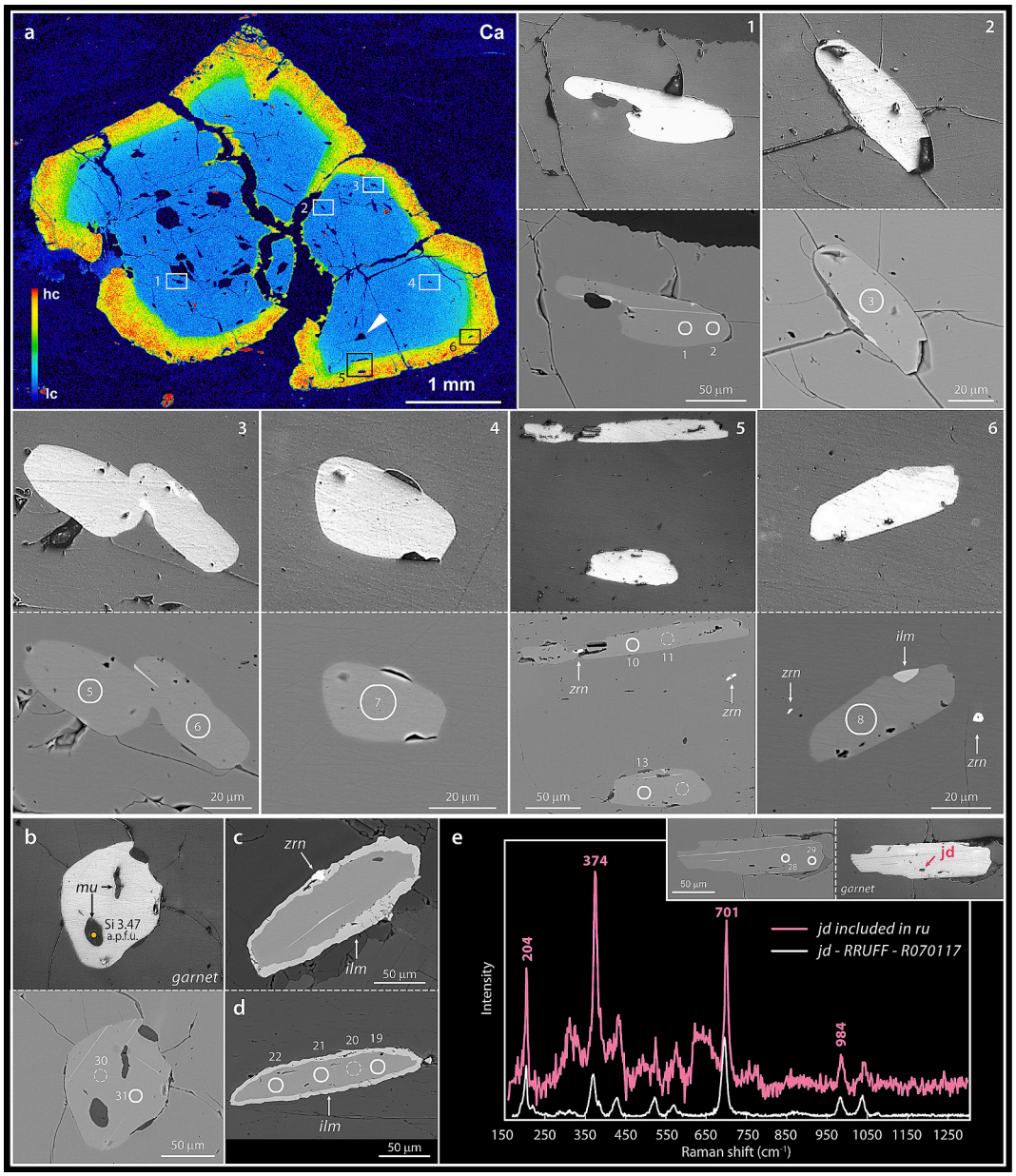

Fig. 4. (a) X-ray map for Ca of a garnet porphyroblast. The location (white and black squares) of the analysed rutile inclusions are shown. Photomicrographs (reflected light) and BSE images of rutile inclusions in a garnet porphyroblast. Note the absence of ilmenite corona in the rutile included in garnet. Ilmenite exsolution lamellae in rutile inclusions are frequently observed when the host garnet around the inclusions is fractured. (b) Si-rich muscovite (Si = 3.47 a.p.f.u.) included in rutile enclosed in garnet. (c,d) Selected rutile grains surrounded by an ilmenite±zircon corona in the muscovite matrix. (e) Raman spectra of jadeite included in rutile (in pink) and reference Raman spectra (in white) for jadeite as displayed in the RRUFF database. Spectra are offset for clarity. Rutile hosting jadeite inclusion is included in garnet outer core (see Fig. S14 in the Supporting Information). White circles (diameter 10 µm) on rutile indicate the position of the analysed spots for U-Pb ages. Dashed white circles on rutile are unsuccessful spots for U-Pb ages due to insufficient radiogenic Pb to extract geochronological information. (For interpretation of the references to colour in this figure legend, the reader is referred to the web version of this article.)

(−3.28 vol%), and lawsonite (−0.69 vol%; Fig. 6a). At peak *P–T* conditions (i.e. 2.8 GPa ~530 °C), the mineral assemblage consists of muscovite (44 vol%), coesite (33 vol%), chloritoid (13 vol%), jadeite (6.9 vol%), garnet (1.1 vol%), lawsonite (1 vol%), and rutile (0.61 vol %).

4.3.2. *Exhumation of the Chasteiran Unit*

The exhumation of the Chasteiran Unit followed a sub-isothermal decompression from 2.7 GPa ~530 °C to 1.5 GPa ~510 °C (Fig. 5d) considering both the effects of fractionation of the garnet cores and possible H_2O undersaturation (Manzotti et al., 2022). This phase diagram was calculated with a fixed amount of H_2O, which was determined so that the proportion of the fluid phase in the rock does not exceed 1 vol % (Thompson and Connolly, 1990). Along this *P–T* path, the modelled amount of chloritoid and jadeite continuously decreases (−13 vol% and − 6.2 vol%, respectively), with chloritoid and jadeite being completely consumed at 1.53 GPa 510 °C and 2.18 GPa 520 °C, respectively (Fig. 6c). Chlorite appears almost at the same conditions of chloritoid breakdown (1.54 GPa 510 °C), whereas paragonite stabilizes at 1.9 GPa 520 °C. Muscovite abundance progressively increases (+3 vol%) up to 1.9 GPa 520 °C and then it remains constant up to 1.5 GPa. Other phases display a more complex behaviour, as detailed below.

During a first stage of exhumation (i.e., from 2.7 GPa 530 °C to 2.1 GPa 520 °C), the modal abundances of lawsonite and glaucophane

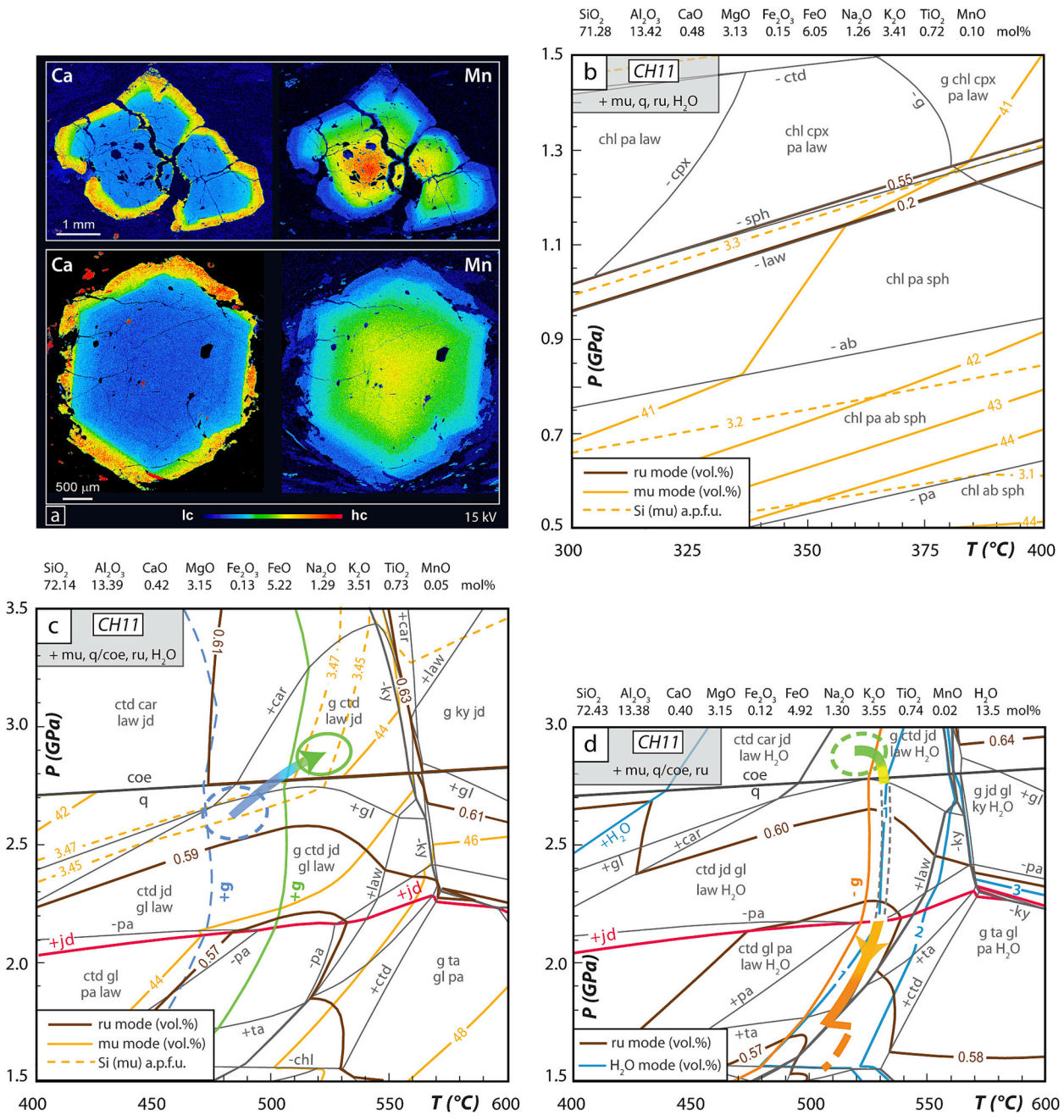

Fig. 5. X-ray maps for Ca and Mn of garnet porphyroblasts (a) and phase diagrams (b,c,d) for sample CH11. (b) H_2O-saturated pseudosection calculated for sample CH11 using the unfractionated bulk-rock composition. (c) H_2O-saturated pseudosection calculated for sample CH11 using the fractionated bulk-rock composition, obtained by subtracting the composition of garnet inner core. The green circle indicates the *P–T* conditions for the growth of the garnet outer core. The position of the garnet-in line and the *P–T* conditions for the growth of the garnet inner core are shown with a blue vertical dashed line and a blue circle, respectively. They were calculated using the unfractionated bulk-rock composition (see Manzotti et al., 2022 for details). Chemical (Si content in muscovite) and modal isopleths (rutile and muscovite) are also shown. (d) *P–T* pseudosection calculated using a fixed amount of H_2O and the bulk-rock composition obtained by garnet core fractionation. Modal isopleths of rutile and H_2O modal are also shown. The multicoloured arrow in (c) and (d) is the inferred *P–T* path followed by the Chasteiran Unit calculated by modelling the garnet growth zoning and the change in its modal amount. The colour of the arrow represents the grossular content of garnet according to the colour bar of the X-ray Ca maps as in (a). (For interpretation of the references to colour in this figure legend, the reader is referred to the web version of this article.)

increase (+0.6 vol% and + 10 vol%, respectively); the modal amount of rutile decreases (−0.03 vol%) whereas the ones of H_2O and garnet are nearly constant (−0.1 vol%). During a second stage of exhumation (i.e. from 2.1 GPa 520 °C to 1.5 GPa 510 °C), the modal abundance of lawsonite progressively decreases (−1.55 vol%) and this phase is completely consumed already at 1.76 GPa 510 °C. Glaucophane modal abundance remains almost constant up to 1.7 GPa 510 °C and then strongly decreases (−6 vol%); rutile modal amount does not change. Garnet modal amount increases (+2.2 vol%), whereas the modal amount of H_2O firstly increases (+0.6 vol%) up to 1.7 GPa and then decreases (−0.4 vol%) up to 1.5 GPa.

Thermodynamic modelling suggests that from 2.7 GPa ~530 °C to 1.5 GPa ~510 °C, there is an overall decrease in modal abundance of rutile (−0.03 vol%), lawsonite (−1.55 vol%), jadeite (−6 vol%), and chloritoid (−13 vol%) and an increase in the modal amount of glaucophane (+4 vol%), muscovite (+3 vol%), garnet (+2.1 vol%), and H_2O

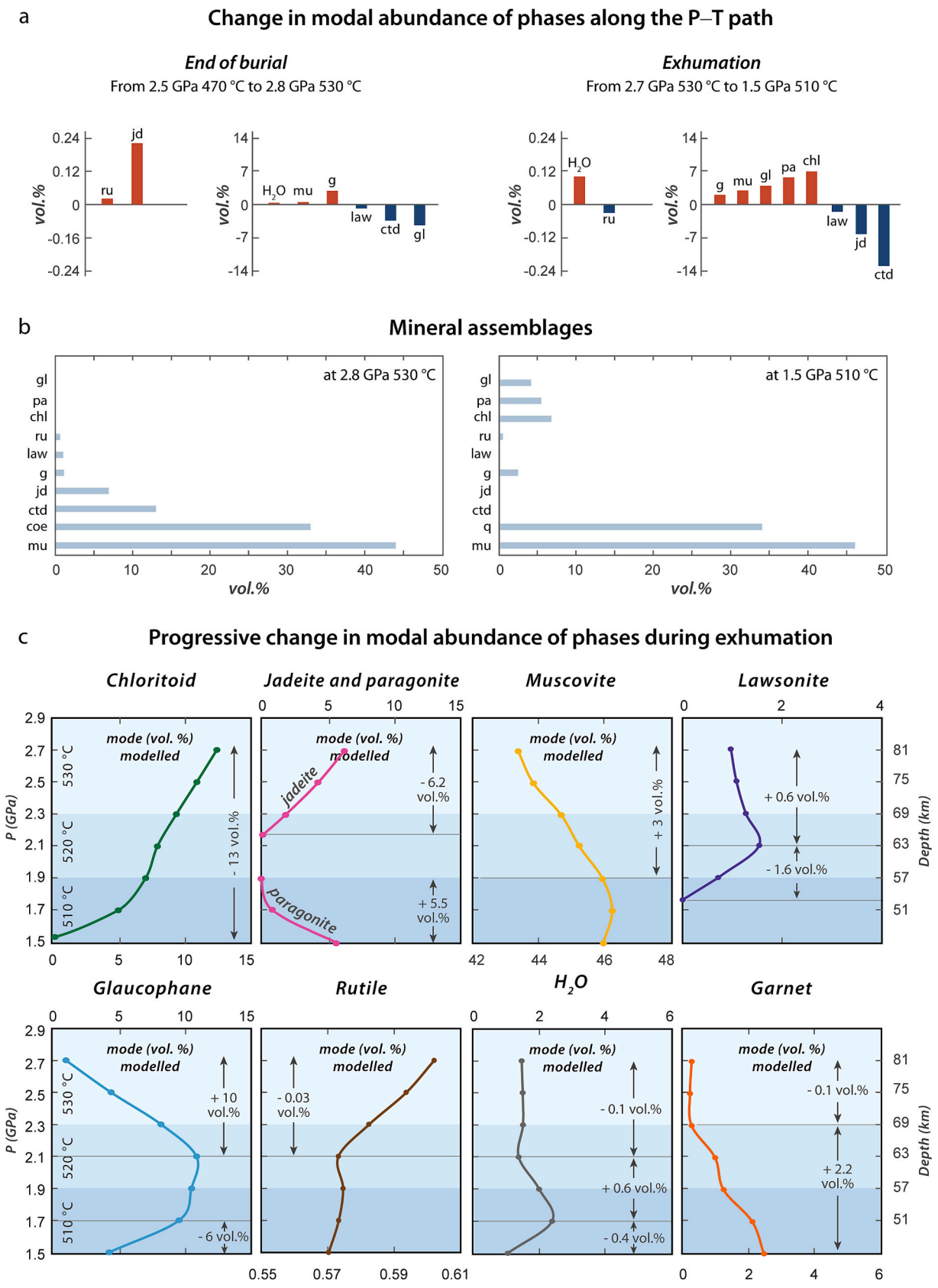

Fig. 6. (a) Change in modal abundance of phases along the inferred *P–T* path. (b) Mineral assemblage at peak *P–T* conditions (2.8 GPa 530C°) and during exhumation (1.5 GPa 510 °C). (c) Progressive change in modal abundance of phases during exhumation. The different shades of blue reflect the change in *T* during exhumation. (For interpretation of the references to colour in this figure legend, the reader is referred to the web version of this article.)

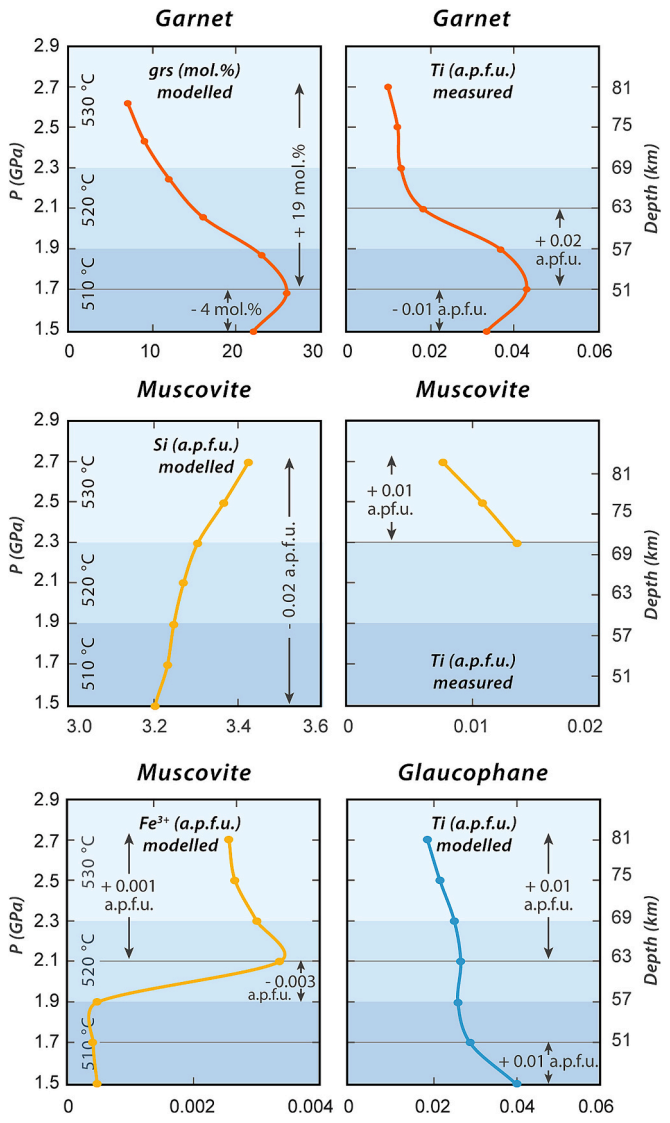

Fig. 7. Progressive change in the chemical composition of garnet, muscovite, and glaucophane along the exhumation path (from 2.7 GPa 530 °C to 1.5 GPa 510 °C). The different shades of blue reflect the change in *T* during exhumation. (For interpretation of the references to colour in this figure legend, the reader is referred to the web version of this article.)

(+0.1 vol%). At 1.5 GPa ~510 °C, the mineral assemblage consists of muscovite (46 vol%), quartz (34 vol%), chlorite (6.9 vol%), paragonite (5.5 vol%), glaucophane (4.2 vol%), garnet (2.5 vol%), and rutile (0.57 vol%; Fig. 6b).

The modelled grossular content of garnet continuously increases (7 mol% - > 26 mol%; +19 mol%) from 2.7 GPa 530 °C down to 1.9 GPa 520 °C, then decreases (26 mol% - > 22 mol%; −4 mol%) from 1.9 GPa 520 °C to 1.5 GPa 510 °C (Fig. 7). Comparison between modelled and measured garnet composition suggests that Ti content in garnet is positively correlated with grossular and displays an increase (+0.02 a.p.f.u.) from 2.7 GPa 530 °C to 1.7 GPa 510 °C followed by a decrease (−0.01. a.p.f.u.) from 1.7 GPa 510 °C to 1.5 GPa 510 °C (Fig. 7).

Along the described exhumation path (i.e. from 2.7 GPa 530 °C to 1.5 GPa 510 °C), the modelled Si content in muscovite continuously decreases from 3.42 a.p.f.u. to 3.21 a.p.f.u. (Fig. 7). The minimum measured Si content is 3.30 a.p.f.u. and corresponds to a modelled *P* of 2.3 GPa at 530 °C. Comparison between modelled and measured muscovite composition indicates that the increase in the measured Ti content (+ 0.01 a.p.f.u.) and Fe^{3+} (+ 0.001 a.p.f.u.) may have occurred during the first stage of exhumation between 2.7 GPa 530 °C and 2.3 GPa 530 °C (Fig. 7).

During the first part of the exhumation path (from 2.7 GPa down to 2.1 GPa), the modelled Ti content in glaucophane increases (+0.01 a.p.f.u.), then it remains almost constant up to 1.7 GPa 510 °C and finally again increases (+0.01 vol%) up to 1.5 GPa 510 °C (Fig. 7). The complete consumption of glaucophane in sample CH11 (only pseudomorphs are observable, see Fig. S7d in Manzotti et al., 2022 for an example) precludes a comparison between the modelled and measured composition of this mineral.

4.3.3. *Rutile and ilmenite stability field during exhumation*

In the investigated sample, rutile is often completely replaced by ilmenite in the chloritoid-rich layers, whereas it only displays ilmenite corona in the muscovite-rich layers. In order to test the hypothesis that local differences in bulk rock chemistry can explain differences in the observed rutile-ilmenite textures, two pseudosections were calculated in the *P–T* range 0.5–1.5 GPa and 400–600 °C (Figs. 8a-b), using two bulk compositions, one of which corresponds to the chloritoid-rich layers (ctd-bulk) and the other to the muscovite-rich layers (mu-bulk). Details on the chemical systems used for these calculations are given in Appendix S3 and Table S8. The two bulk rock compositions mainly differ in their total iron (ctd-bulk: 14.45 wt%, mu-bulk: 7.97 wt%) and sodium (ctd-bulk: 0.42 wt%, mu-bulk:1.85 wt%) contents. Following previous calculations aimed to model the exhumation history (Manzotti et al., 2018; Manzotti et al., 2022), the phase diagrams were calculated with a fixed amount of H_2O, corresponding to 1 vol% at peak *T*. The fraction of Fe^{3+} was set to 5 wt% of the total Fe [X (Fe^{3+}) = Fe^{3+}/Fe_{total}], considering the absence of Fe^{3+}-rich oxides (hematite and magnetite), the absence of Fe^{3+} in ilmenite, the limited modal amount of epidote and the negligible amount of Fe^{3+} in garnet (see also Manzotti et al., 2018 and Manzotti et al., 2024 for the rationale). In addition, *P–X*(Fe_2O_3) pseudosections were also calculated for the ctd- and mu-bulk compositions in the *P* range 0.5–1.5 GPa at 500 °C in order to test the sensitivity of the modelled results with respect to the assumed Fe^{3+} content and specifically to explore the effect of oxidation state of the rock on the stability of ilmenite. A detailed description of these diagrams is given in the Appendix S4.

Compared to the phase diagram calculated using the mu-bulk, the ctd-bulk results in (i) the stabilization of ilmenite toward high *P* at *T* < 550 °C, (ii) the presence of H_2O in the entire investigated *P–T* space, (iii) the stabilization of biotite only at *T* > 550 °C and *P* of 0.5–0.8 GPa, and (iv) the absence of paragonite at *P* < 1.4 GPa and of garnet at *T* < 520 °C (Fig. 8a). In both diagrams, rutile disappears at *T* > 500 °C whereas titanite is not stable, probably due to the low bulk calcium content.

In the pseudosection calculated for the ctd-bulk system composition, a *P–T* evolution involving cooling and decompression would occur at H_2O-present conditions and would result in the replacement of rutile by ilmenite at relatively high *P* (already at 1.5 GPa, Fig. 8a). Conversely, in the pseudosection calculated for the mu bulk system composition, a similar *P–T* evolution would result in H_2O-absent conditions at 1.2 GPa ~500 °C, thus limiting retrogression during decompression. Ilmenite would stabilize at lower *P* (i.e. ~1.1 GPa at ~500 °C) compared to the ctd-rich layers (Fig. 8b). These observations suggest that the differences in rutile-ilmenite textures observed between the ctd- and mu-rich layers may be attributed to differences in the local bulk composition, with the ilmenite stability field being controlled by the total iron content.

4.4. *Geochronology*

4.4.1. *Garnet age (sample CH11)*

Four hundred-thirteen analyses were performed on a total of 22 garnet crystals. Overall, garnet cores show U contents in the range 3–73 ng/g (Fig. 9a, Table S11) with no significant variations within crystals (with the exception of one single garnet core, Figs. S10-S12). Specifically, most of the spot analyses (240 out of 280) are in the range 5–20

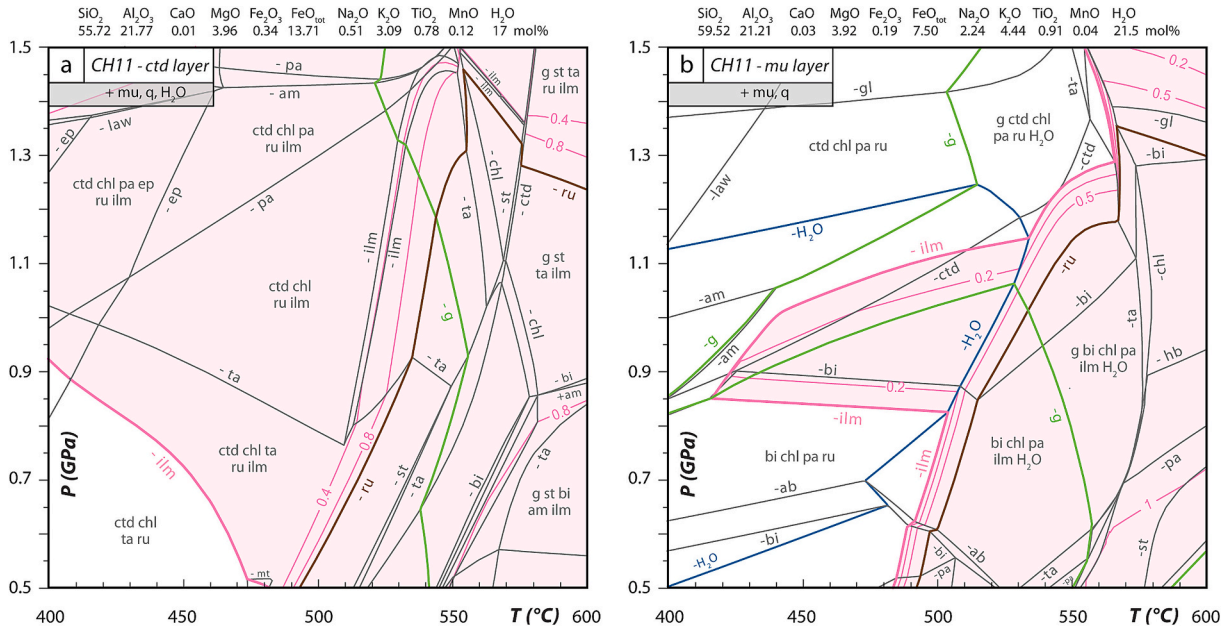

Fig. 8. *P–T* pseudosections calculated for sample CH11 with a fixed amount of H_2O and using the system composition of the chloritoid- (a) and muscovite-rich (b) domains. The pale-pink field indicates the *P–T* space where ilmenite is stable. Please note that given the very small amount of CaO in the local bulk compositions used for calculating these diagrams, titanite does not grow at low *P–T* conditions. (For interpretation of the references to colour in this figure legend, the reader is referred to the web version of this article.)

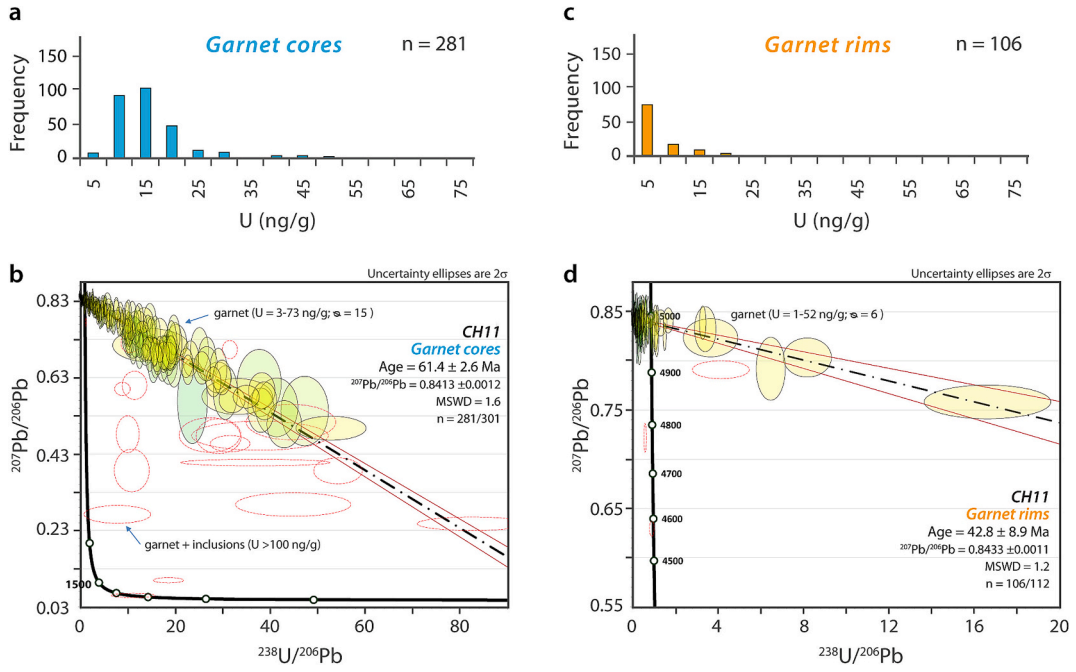

Fig. 9. (a,c) Measured U content (histograms) for the U-Pb spots analysed in garnet cores and rims. (b,d) Tera-Wasserburg diagrams with lower intercept garnet U-Pb dates for sample CH11. (b) garnet cores, (d) garnet rims. Colour code refers to the measured U content (green tone = low U concentration, yellow tone = high U concentration). See Figs. S11-S12 and Appendix S1 for spot locations and geochronological dates, respectively. (For interpretation of the references to colour in this figure legend, the reader is referred to the web version of this article.)

ng/g. The U/Pb data plotted in a Tera-Wasserburg diagram define a regression line with a lower intercept date of 61.4 ± 2.6 Ma (MSWD = 1.6; n = 280), and an upper intercept corresponding to a typical terrestrial $^{207}Pb/^{206}Pb$ value of 0.8413 ± 0.0012 (Fig. 9b; cf. Stacey and Kramers, 1975).

Garnet rims are richer in initial Pb than the cores and display very low U concentrations (U_{avg} = 6 ng/g; 106 out of 112 spot analyses; Fig. 9c, Table S11). Elevated U contents (>52 ng/g; 6 out of 112 spot analyses) was measured in the rims of two garnet crystals characterized by numerous rutile inclusions as well as in a few spots performed close to rutile inclusions (Figs. S10-S12). These analyses were rejected from age calculations. The U-Pb data plotted in a Tera-Wasserburg diagram define a regression line with a lower intercept date of 42.8 ± 8.9 Ma (MSWD = 1.17; n = 106) and an upper intercept corresponding to a typical terrestrial $^{207}Pb/^{206}Pb$ value of 0.8433 ± 0.0011 (Fig. 9d).

4.4.2. Rutile age (sample CH11)

Eighty-eight analyses were performed on a total of 50 rutile crystals. 45 analyses out of 88 return meaningful data that were used for U-Pb geochronology. U content varies within grains, but there is no straightforward relation between U content and crystal size, crystal shape and/or microstructural setting (see Appendix S1). Rutile included in garnet generally displays a decrease in common Pb toward the rims of the grains.

All the common Pb uncorrected data plotted in a Tera-Wasserburg diagram define a free regression with a lower intercept date of 35.5 ± 3.8 Ma with an MSWD of 2. Omitting a single outlier (marked by italic fonts in the Appendix S1 and shown as a red empty dashed ellipse in Fig. 10) gives a statistically valid line (MSWD 1.3, probability 0.08) and a date of 36.8 ± 4.1 Ma (Fig. 10). In both cases, the upper intercept corresponds to a typical terrestrial $^{207}Pb/^{206}Pb$ value of 0.85 ± 0.04 (or 0.02 with the better regression).

However, a careful inspection of the Tera-Wasserburg diagram reveals a spread in the distribution of the ellipses which may suggest a progressive younging in the dates (Figs. 10a and S16). The oldest dates have the highest proportion of common Pb, but the smallest errors. The youngest dates display variable common Pb and large errors. We do not identify any straightforward relations between dates and petrographic mode of occurrence (i.e. microstructural setting, rutile texture and chemistry; Appendix S1).

4.4.3. Detrital zircon geochronology (sample CH43)

U-Pb dates were measured on 120 zircon grains, that were different both in terms of grain size and shape. Most zircon grains are prismatic and inclusions-free (up to 120 μm in size); they show oscillatory zoning (Fig. 11a), variable Th/U ratio (in the range 0.1–1.0) and a thin rim (< 5 μm). Ten grains are sub-rounded and display homogenous bright or dark luminescence and low Th/U ratio (< 0.1). A few other grains display partially dissolved (inherited) cores surrounded by overgrowth. Five overgrowths were analysed and yield low Th/U ratio (< 0.1). They are therefore interpreted as metamorphic (e.g., Teipel et al., 2004) and yield apparent ages ranging between 1956 and 456 Ma (Fig. S17).

Concordant data (118 out of 120 analyses) range from Neoarchean (2692 ± 13 Ma) to Upper Ordovician (456 ± 15 Ma), with the majority of dates in the range 1000–450 Ma and only a few scattered dates older than 1000 Ma (Fig. 11b). The age spectrum is dominated by a main age peak at ~630–600 Ma (50 Ediacaran analyses), whereas the peak at 480–450 Ma (12 Ordovician analyses) represents the youngest zircon cluster. Subordinate peaks are at ~550 Ma (Cambrian), ~680–660 Ma (Cryogenian), and 1000–950 Ma (Tonian). The youngest magmatic concordant date is Ordovician (462 ± 16 Ma; Th/U = 0.32). If we calculate a weighted mean age using the ten youngest concordant analyses (removing the young date that is <90 % concordant) we obtain a date of 470 ± 5 Ma (MSWD = 1.2).

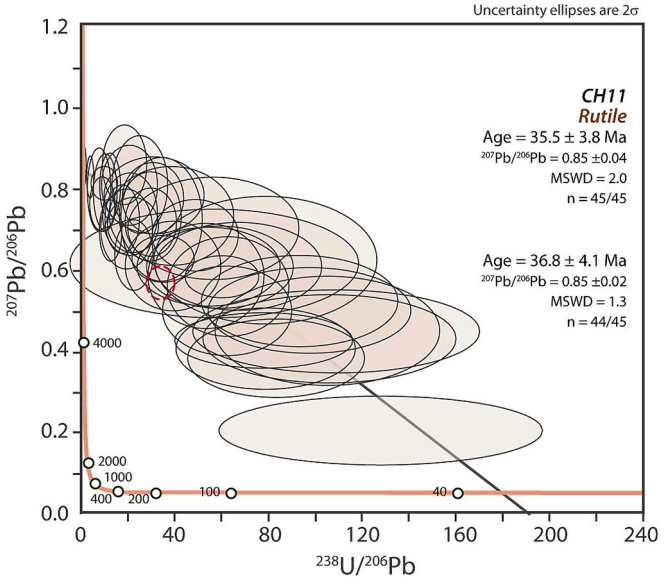

Fig. 10. Tera-Wasserburg diagrams for U-Pb analyses of rutile, uncorrected for initial Pb. See Figs. S13-S15 and Appendix S1 for spot locations and geochronological dates, respectively.

5. Discussion

5.1. Maximum depositional age of the Chasteiran metasediments

There is no evidence that the sediments experience pre-Alpine high-grade metamorphism after their deposition (Manzotti et al., 2022), a process that may result in Pb loss giving apparent (disturbed) ages of detrital cores younger than the real depositional age. According to detrital zircon geochronology, the maximum depositional age of the protolith of the Chasteiran micaschist is at ~470 Ma. Two main sources have been identified for the detrital material, the most abundant one at ~600 Ma (i.e. Ediacaran) and a minor component at ~470 Ma. These results are (i) very different from those obtained in the underlying Pinerolo metasediments that contain a dominant population of Carboniferous (~330 Ma) zircon grains (Manzotti et al., 2016); (ii) similar to those obtained in the overlying Muret Unit, although the Ordovician population is better represented in the Chasteiran micaschist than in the samples from the Muret Unit (Nosenzo et al., 2022; Nosenzo et al., 2024). Another interesting point is that the Ordovician zircon population in the Chasteiran micaschist is older than the Ordovician protolith ages of the immediately overlying Granero Orthogneiss (447 ± 1 Ma, 456 ± 2 Ma and 440 ± 2 Ma; Nosenzo et al., 2024). We conclude that the latter cannot be the source of the Ordovician zircon grains in the sedimentary protolith of the Chasteiran micaschist. Manzotti et al. (2022) have hypothesized a potential Silurian age for the Chasteiran sediment which is still valid given the geochronological dates obtained in this study.

5.2. Relative timing of growth and consumption of garnet and rutile

A key element for interpreting garnet and rutile dates is a proper understanding of their growth history. Thermodynamic modelling was already applied to the Chasteiran micaschist (Manzotti et al., 2022), with the main aim of constraining *P–T* conditions. In the present study, we provide a closer look at the thermodynamic modelling, in order to better understand the growth and dissolution history of garnet in relation to the other phases, especially rutile. This allows identifying the elemental exchange between these phases, and their potential implications for dating.

5.2.1. Garnet growth

Thermodynamic modelling suggests that *garnet cores* grew during the final stage of burial, from 2.5 to 2.7 GPa 470–500 °C to 2.7–2.8 GPa 510–530 °C, in the quartz and coesite stability field. Model predictions (i.e. the garnet mode isopleths) and textural observations indicate that garnet was only marginally consumed (−0.1 vol%) during an early stage of isothermal decompression (from 2.8 GPa to 2.3 GPa at ~530 °C), also characterized by a minor growth of lawsonite and fluid consumption (Fig. 6c). The growth of *garnet rims* was predicted to occur (see Manzotti et al., 2022) during a second stage of exhumation along a nearly isothermal decompression (from 2.8 GPa to 1.5 GPa at ~510 °C), an interval that has been better defined in this study from 2.3 GPa to 1.5 GPa at ~510 °C, considering the garnet isomodes (Figs. 5d and 6c). In this *P* interval, garnet growth is accompanied by lawsonite (~1.6 vol%) and chloritoid (~10 vol%) consumption coupled with fluid production (Fig. 6c). The local presence of porosity in garnet rims, as well as the patchy Ca-distribution also suggests that its growth occurred in the

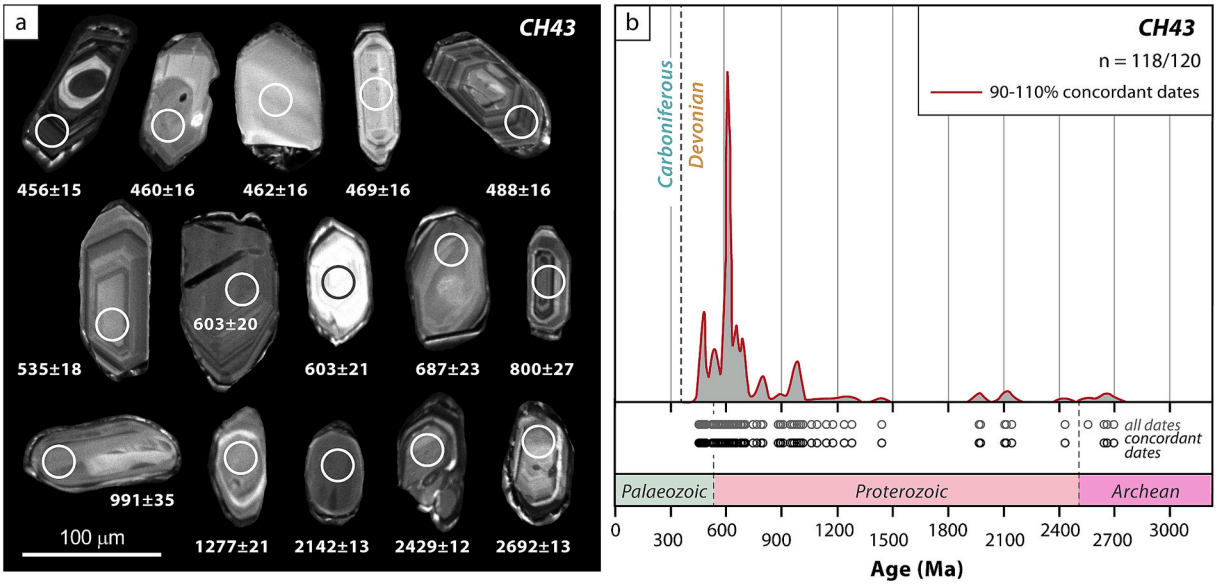

Fig. 11. (a) Cathodoluminescence (CL) images of representative zircon crystals from sample CH43. White circles (diameter 25 μm) indicate the position of the analysed spots for U-Pb ages. Single spot analyses are given as $^{207}Pb/^{206}Pb$ ages for results older than 1 Ga and $^{206}Pb/^{238}U$ ages for results younger than 1 Ga. (b) Detrital zircon age distribution represented with Kernel density estimate (KDE). Individual data are represented with empty circles at the base of the diagram.

presence of a fluid phase. The latter was in equilibrium with the chemical composition of garnet cores as proved by the regularly shaped interface between garnet outer cores and rims with only rare and small embayments.

5.2.2. *Textural evidence for rutile stability*

Textural observations show that rutile is found both as inclusions in garnet and in the matrix. Rutile is largely replaced by ilmenite in the matrix, with ilmenite coronas growing around rutile cores. This texture is never observed when rutile is included in garnet cores as well as in garnet rims, although rare and thin ilmenite lamellae may be present in some rutile inclusions. These observations suggest that rutile was stable during the entire history of garnet growth, and reacted to ilmenite in the matrix after garnet growth. Caution must, however, be taken, because the presence of rutile during a large segment of the *P–T* path does not imply that this mineral was inert. In a continuously deforming matrix, rutile may have been affected by solid state (i.e. volume) diffusion (Cherniak, 2000) and recrystallization (by dissolution-precipitation or even plastic, intracrystalline, deformation; e.g., Moore et al., 2020; Verberne et al., 2022). Moreover, its modal proportion may have changed in a given mineral assemblage, provided Ti incorporation into coexisting phases was possible. To better elucidate these dynamic processes, we hereafter combine the thermodynamic model predictions with detailed chemical mapping.

5.2.3. *Rutile growth during burial*

Thermodynamic modelling predicts that rutile grew as result of titanite breakdown during prograde metamorphism, mainly between 0.95 and 1.3 GPa and 300–400 °C and contemporaneously with lawsonite growth, before the onset of garnet growth. The geometry of rutile isomodes indicates that its modal amount is a function of *P* rather than *T*, at least at $P < 1.5$ GPa (Fig. 5b). We understand that the exact location of the transition from titanite to rutile is dependent from the precise composition of titanite and lawsonite, because these two phases may incorporate small amounts of Al and Fe^{3+}, respectively. Our modelling considers the two minerals as pure phases, and therefore the width and the position of the multivariant field where titanite, rutile and lawsonite coexist may change. However, this is not considered significant, the main lesson from the thermodynamic modelling being that rutile appears much earlier than garnet, a fact that is fully consistent with the textural observations.

Because rare jadeite and Si-rich muscovite inclusions are observed in rutile (stable at a minimum *P* of 2.0 GPa and 2.3 GPa, respectively), we infer that at least some grains either grew or recrystallised (by dissolution-precipitation) at a *P* higher than 2.0 GPa, in equilibrium with garnet cores. No evidence for rutile recrystallization due to plastic deformation, a poorly documented process so far (Zack and Kooijman, 2017), has been found in the studied micaschist.

5.2.4. *Rutile dissolution during exhumation*

Thermodynamic modelling indicates that rutile dissolution took place during exhumation along a nearly isothermal decompression (from 2.8 GPa to 2.1 GPa, Figs. 5d and 6c). Evidence for rutile dissolution is scanty, given the small amounts involved, and may be recorded by the elemental exchanges between rutile and coexisting phases (garnet, muscovite, glaucophane), or evaluated considering the model predictions. These two approaches are not exactly symmetrical, because the solid solution models we have used for garnet and muscovite do not consider Ti, contrary to glaucophane, which is unfortunately pseudomorphed in the studied sample.

In our case, garnet cores are characterized by low-Ca content and the near absence of Ti. Conversely, garnet rims display higher Ca and Ti contents than garnet cores. Recent studies (e.g., Ackerson et al., 2017) demonstrated a positive correlation between Ca and Ti incorporation in garnet, suggesting that Ti solubility in garnet is strongly influenced by grossular content. A potential source for the increase of Ti content in garnet rims is indeed the dissolution of rutile.

Concerning muscovite, we note that, according to our chemical and textural observations (Fig. 3), the Si content is higher in the cores (Si = 3.40–3.47 a.p.f.u.) compared to the rims (Si = 3.30–3.37 a.p.f.u.). The Ti content in muscovite is low (< 0.28 wt%), and is negatively correlated with Si content (from 0.0063 in the cores to 0.0141 a.p.f.u. in the rims). Thermodynamic modelling indicates that muscovite rims grew during a near isothermal decompression (from 2.8 GPa ~530 °C to ~2.1 ~510 °C). The Ti source in the rims may be again identified in the dissolution of rutile.

Another facet of the Ti partitioning between coexisting phases is provided by thermodynamic modelling, indicating that the Ti released by rutile consumption was primarily accommodated in amphibole (glaucophane, Fig. 7). Because glaucophane is now completely

pseudomorphed in the studied sample, we are not able to quantify this process.

Overall, rutile growth has taken place at increasing *P* during burial. During decompression, rutile dissolution occurs before its replacement by ilmenite, as predicted by thermodynamic modelling. Dissolution, which is responsible for a small decrease of rutile mode (from 0.61 vol% at peak *P–T* conditions to 0.57 vol% at 2.1 GPa ~520 °C), may have provided the source for Ti in glaucophane (according to our thermodynamic modelling), garnet rims and muscovite rims, as observed in the studied rock.

Finally, matrix rutile was partially transformed to ilmenite during decompression and exhumation of the Chasteiran Unit. This reaction involved the consumption of Fe-bearing phases (e.g., chloritoid, garnet, amphibole). We show that the *P* at which this transformation took place is strongly dependent on the local bulk composition, occurring at ~1.5 GPa in the chloritoid-rich domain and at ~1.1 GPa the muscovite-rich domain.

5.3. Interpretation of garnet and rutile ages

In an ideal system, grain size and cooling rates control the closure temperature (T_c) of a radiogenic system and therefore the measured age (i.e., the Dodson equation, Dodson, 1973). However, several parameters may significantly affect the T_c of the dated mineral, namely thermal overprint, plastic deformation, fluid pulses… (e.g., Bosse and Villa, 2019; Villa, 1998). As a first-order statement, the garnet U-Pb dates from the investigated Chasteiran micaschist can be interpreted as growth ages because the U-Pb system in garnet has a very high T_c (> 800 °C Mezger, 1989; > 1100 °C Dahl, 1997). Interpretation of the rutile data is less straightforward, because the T_c for U-Pb in rutile is largely disputed, with values ranging from 400 °C to 600 °C (see Kooijman et al., 2010; Zack and Kooijman, 2017 for a review), coinciding with the range of estimated metamorphic *T* for our sample.

5.3.1. Garnet ages

LA-ICP-MS U-Pb geochronology of garnet is becoming a well-established technique for dating metamorphic/metasomatic processes in skarns, probably because the andraditic garnet so characteristic of the skarns contains a rather large amount of U (c. 2000–5000 ng/g: see Table S12). In metapelites, where almandine-pyrope garnet is stable over a large range of *P–T* conditions, the amount of U in garnet is much smaller (typically <100 ng/g: see Table S12). However, technological advances now allow dating such low U garnets, and have already provided robust and meaningful dates in several metamorphic terrains (e.g., Bartoli et al., 2024; Millonig et al., 2020; Shu et al., 2024).

U-Pb dating of our sample indicates two distinct stages of growth for garnet cores and rims at 61.4 ± 2.6 Ma and 42.8 ± 8.9 Ma, respectively. In the studied sample, garnet crystals display inclusions large enough to be detected and avoided during geochronological investigation. The presence of (i) coesite in the garnet outer cores, not in the rims and (ii) chloritoid and rutile in the garnet cores coupled with thermodynamic calculations rule out the hypothesis that garnet cores are pre-Alpine and thus garnet from the Chasteiran micaschist are not multistage crystals associated with two orogenic cycles (see Manzotti et al., 2022 for details), in which case interferences between the two garnet generations needs special attention. Such a polycyclism has been documented by Lu-Hf dating of multistage garnet from the Adula nappe in the central Alps (Herwartz et al., 2011). Another potential source of mixed ages could be linked with the occurrence of older zircon grains, not exposed at the surface of the sample, but evaporated when the laser beam penetrated deeper inside the garnet. For this reason, we excluded analyses with a U content significantly higher than the vast majority of the analyses (shown in red in Figs. S10-S12), considering that they may have been contaminated by micro-inclusions (Millonig et al., 2020).

Garnet cores and rims show distinct and consistent compositions that reflect their growth at different *P–T* conditions during the Alpine orogeny, as supported by thermodynamic modelling. Considering that there is no evidence for mixing between pre-Alpine and Alpine dates, and no large scatter of datapoints away from the regression line in the TW plot, we therefore interpret the date at 61 ± 3 Ma as the early growth of garnet occurring during the final stage (from 2.5 GPa to 2.8 GPa) of prograde metamorphism and burial of the Chasteiran Unit (Fig. 12).

Garnet rims display higher common-Pb concentrations than garnet cores (U/Pb ratios are lower) and U-Pb dates obtained on this domain have lower analytical precision and greater age uncertainties than the garnet cores. Nevertheless, they constrain the growth of garnet rims at 43 ± 9 Ma, indicating that garnet cores and rims grew during two distinct stages. The time interval separating the growth of garnet cores and rims is consistent with our thermodynamic modelling, which indicates the absence of garnet growth during the initial stage of exhumation, between 2.7. GPa and 2.3 GPa and constrains the growth of garnet rims between 2.3 GPa and 1.5 GPa during a nearly isothermal decompression at ~510 °C (Fig. 12).

5.3.2. Rutile age(s)

SIMS U-Pb dating of rutile, irrespective of its petrographic mode of occurrence, yields a date of 36.8 ± 4.1 Ma. Overall, the rutile date is younger that the garnet cores date (~61 Ma) and equivalent within error to the garnet rims date (~43 Ma). However, as pointed out above, the rutile dates show a considerable spread that warrants a careful discussion. Textural relations indicate that rutile growth preceded or was contemporaneous with the crystallization of garnet cores. Rutile dates are therefore expected to yield similar values as the garnet cores. However, several lines of evidence suggest that rutile re-equilibrated during cooling and decompression.

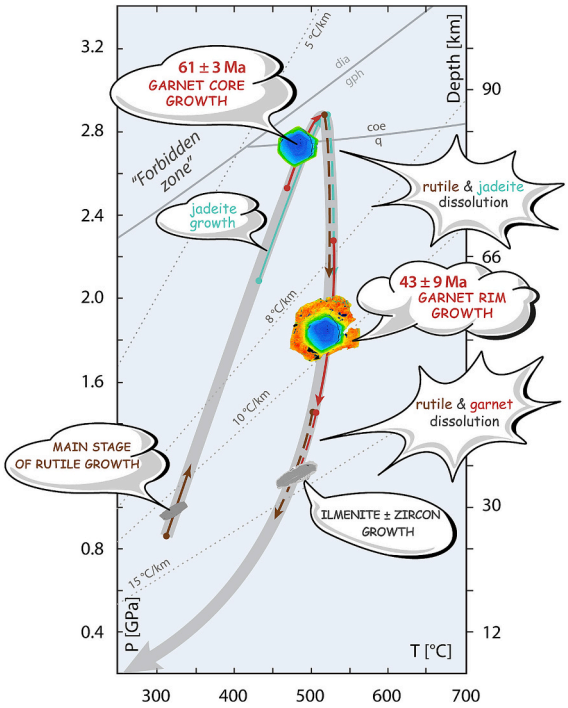

Fig. 12. Inferred *P–T–t* path for the Chasteiran Unit in the northern Dora-Maira Massif. Stages of growth and dissolution for key minerals are reported as well as calculated ages for garnet cores and rims. Note that the titanite-rutile transition is based on thermodynamic modelling for pure phases. Red continuous lines indicate periods of garnet growth. A first period of growth (garnet core) occurred at increasing *P* and *T* at ~61 ± 3 Ma. A second period of growth (garnet rim) took place after a significant amount of decompression at ~43 ± 9 Ma. (For interpretation of the references to colour in this figure legend, the reader is referred to the web version of this article.)

Inclusions of rutile in garnet are commonly surrounded by fractures and some crystals display ilmenite exsolution lamellae, indicating that they were not fully armoured within garnet and may have behaved as an open system after initial crystallization (e.g. Bosse and Villa, 2019; Clark et al., 2024; Shu et al., 2024). Resetting of the U-Pb system in rutile may have occurred not by volume diffusion, as experimentally investigated (Cherniak, 2000), but through elemental diffusion and mass transport/transfer in the intergranular aqueous fluid, a process that is orders of magnitude faster than intracrystalline diffusion (e.g., Grand'Homme et al., 2016; Williams et al., 2011).

Evidence for the presence of a fluid phase are multiple. Phase diagrams aimed to model the exhumation *P–T* path of the Chasteiran Unit has been calculated without the addition of a water-rich fluid during decompression, i.e. with the same amount of water than at peak *P–T* conditions. Despite this restrictive condition, the modelling indicates that a fluid phase was present in the studied rock during decompression, mainly linked to lawsonite and chloritoid breakdown. Patchy zoning of Ca in garnet rims, and the presence of pores may be considered additional evidence for the presence of a fluid phase during decompression.

Finally, the presence of a late fluid is also suggested by the texture of some rutile grains in the matrix, that are replaced by oxides (ilmenite) + silicates (i.e. zircon). This texture indicates that rutile was consumed with a consequent Zr release in the presence of silica. This process cannot be the result of a solid-state diffusion of elements, but it must have taken place in the presence of a fluid phase, in which Zr was poorly soluble. The newly grown zircon spatially associated with the corona reaction around rutile suggests that the Zr released from rutile during the decompression reaction was re-distributed in newly zircon crystals rather than in ilmenite. This can be explained by the limited ability of ilmenite to accommodate Zr in the crystal lattice during retrograde metamorphism (e.g., Sláma et al., 2007) and results in a significantly lower content of Zr in ilmenite with respect to rutile.

In this respect, the nucleation and growth of zircon during metamorphic reactions along the exhumation *P–T* path observed in the investigated sample has been documented by previous studies (e.g., Austrheim et al., 2008). In particular, the Zr release from rutile during decompression and cooling has been predicted by thermodynamic investigations (e.g., Kohn et al., 2015) and reported in several metamorphic terranes (e.g., Bingen et al., 2001; Sláma et al., 2007).

5.4. Summary and potential tectonic implications

In contrast to the southern Dora-Maira Massif, few geochronological studies have been performed in the northern Dora-Maira Massif, so far (Angiboust and Glodny, 2020; Scaillet et al., 1992). The isotopic data on white mica obtained by Scaillet et al. (1992) are difficult to interpret because of excess ^{40}Ar, as clearly discussed by the authors (Scaillet, 1996). The Rb-Sr data of Angiboust and Glodny (2020) were interpreted by the authors as dating some stage along the exhumation path. Therefore, our study represents the first attempt to constrain the timing of the peak *HP/UHP* metamorphism in the northern Dora-Maira Massif, using a multichronometer approach coupled with thermodynamic modelling.

On the basis of our textural, petrological, and geochronological data, we conclude that rutile grew during prograde metamorphism (mainly between 0.9 GPa and 1.3 GPa) mainly at the onset of burial of the Chasteiran Unit. The growth of garnet cores occurred between 2.5 GPa and 2.8 GPa and the end of burial at 61 ± 3 Ma. Garnet rims grew at fluid-present conditions during a nearly isothermal decompression between 2.3 GPa and 1.5 GPa at 43 ± 9 Ma. We interpret the rutile dates as representing the average of a metamorphic continuum during which a fluid phase was present, rather than the absolute timing of a geologic event.

Interestingly, the timing of the *HP* metamorphism in the Gran Paradiso and the Monte Rosa Massifs (i.e. ~42–45 Ma; Lapen et al., 2007; Manzotti et al., 2018) coincides within the error with the growth of garnet rims in the Chasteiran Unit and occurred at similar *P–T* conditions (i.e. 1.8–2.0 GPa, 500–520 °C). However, due to the large uncertainties on the timing of the garnet rims growth in the studied sample, we consider any estimation of exhumation rates on the basis of these data as premature.

With respect to the tectonic evolution of the Western Alps, some remarks are useful. Firstly, the simplest (therefore the most elegant and robust) model is to consider that, at plate scale, oceanic subduction should predate continental subduction. We would therefore expect (i) similar ages for units occupying the same structural position, and (ii) older ages in the oceanic units (Monviso, Orsiera-Rocciavrè) compared to the Dora-Maira Massif. In this regard, our results may suggest a different timing of burial and exhumation for the northern and southern Dora-Maira Massif (see Bonnet et al., 2022 and refs therein for a review). The age of metamorphism in the southern Dora-Maira Massif has been investigated using different chronometers. Duchêne et al. (1997) obtained a garnet-whole rock Lu-Hf isochron, yielding a date of 32.8 ± 1.2 Ma, recalculated to 34.1 ± 6.0 Ma with the ^{176}Lu decay constant of Söderlund et al. (2004). This date has been interpreted as the timing of the *UHP* metamorphism in the Brossasco-Isasca Unit. We cannot exclude that older U-Pb garnet ages (~60 Ma) similar to the one of the *UHP* Chasteiran Unit can be also obtained in the southern Dora-Maira Massif. With respect to this, it is worth to note that monazite inclusions in pyrope from the whiteschist of the *UHP* Brossasco-Isasca Unit yielded an old chemical date of ~60 Ma, interpreted as the timing of prograde metamorphism during burial (Vaggelli et al., 2006).

Our data also imply that the peak *UHP* episode in the northern Dora-Maira Massif is older than the peak eclogite-facies in the overlying oceanic units. For example, in the Viso Massif U-Pb zircon geochronology yielded dates of 45 ± 1 Ma (Rubatto and Hermann, 2003), 45.8 ± 0.7 Ma (Rubatto and Angiboust, 2015), and 51 ± 1 Ma (Garber et al., 2020). Garnet-whole rock Lu-Hf isochron has provided a date of 49.1 ± 1.2 Ma (Duchêne et al., 1997). These dates are considered to represent the timing of the peak eclogite facies metamorphism.

Pending further investigations aimed at clarifying this point in the continental units, the departure from the simplest model alluded to above may also result from complexities of two distinct orders.

A first complexity is related to the geometry of the subducted margin before its subduction. Assuming that the Briançonnais palaeomargin bears the characteristics of the so-called hyperextended margins (e.g., Decarlis et al., 2015), we may expect the occurrence of small-sized volumes of continental crust belonging to different extensional allochthons and entering the subduction zone at different times.

A second complexity may be added, because the different blocks may have detached from the downgoing slab at different times, i.e. depths, adding a new variable in the *P–T–t* path of the individual blocks that are now stacked together. In such a case it would be rather useless to try to put all the units in strict correspondence from a petrological-geochronological perspective. Our results should invite the reader to some caution with respect to tectonic models, and promote further research aimed at clarifying these issues. At last, one should remember that subduction in the Western Alps is first documented in the Sesia-Dent Blanche Nappes, at about 60–80 Ma (Manzotti et al., 2014 and refs therein; Gilotti et al., 2023; Vho et al., 2020), i.e. well before the accepted ages for the subduction of the Piemonte-Liguria Ocean (Manzotti and Ballèvre, 2024 and refs therein). Although the Sesia Zone is not cropping out along the studied traverse (being covered by the Plio-Quaternary of the Po plain), and therefore generally ignored in tectonic models along this traverse, ages of c. 60 Ma for subduction of a piece of the Briançonnais palaeomargin are reasonable.

6. Conclusions

This study provides new U-Pb ages from zircon, garnet, and rutile from the Chasteiran Unit in the northern Dora-Maira Massif (Western Alps).

- Detrital zircon geochronology constrains the maximum depositional age of the protolith of the Chasteiran micaschist at ~470 Ma and reveals a major source of detrital material at ~600 Ma. Zircon does not record substantial resetting during the Alpine orogeny.
- Thermodynamic modelling and U-Pb dating indicate two main stages for garnet growth. The garnet cores grew at the end of the burial history (2.5–2.8 GPa at 470–530 °C) at 61 ± 3 Ma, while the garnet rims record a second stage of growth during a nearly isothermal exhumation (2.3 GPa 520 °C and 1.5 GPa 510 °C) at 43 ± 9 Ma.
- The main stage of rutile growth is constrained between 0.9 and 1.3 GPa by thermodynamic modelling and continued up to the end of burial as suggested by inclusions of jadeite and Si-rich muscovite. Its growth has mainly taken place before the beginning of garnet growth. U-Pb dating of rutile, irrespective of its petrographic mode of occurrence, yields a date of 37 ± 4 Ma, suggesting that this mineral was partially re-equilibrated during exhumation.

Financial support

This work was financially supported by the Carl Trygger Foundation (grant no. CTS21:1301 to Paola Manzotti) and by Stockholm University.

Authors contribution

Fieldwork and samples collection by PM and MB. The draft manuscript and figures were prepared by PM and finalised after input and edits provided by co-authors. Manuscript conceptualization by PM and MB with input from co-authors.

CRediT authorship contribution statement

Paola Manzotti: Writing – original draft, Visualization, Validation, Project administration, Investigation, Funding acquisition, Formal analysis, Data curation, Conceptualization. **Leo J. Millonig:** Writing – review & editing, Methodology, Data curation. **Axel Gerdes:** Writing – review & editing, Methodology, Data curation. **Martin J. Whitehouse:** Methodology, Data curation. **Heejin Jeon:** Methodology, Data curation. **Marc Poujol:** Writing – review & editing, Visualization, Validation, Methodology, Data curation. **Michel Ballèvre:** Writing – review & editing, Visualization, Validation, Investigation.

Declaration of competing interest

The authors declare that they have no known competing financial interests or personal relationships that could have appeared to influence the work reported in this paper.

Acknowledgements

We thank Mikaela Krona and Francesco Nosenzo for their help with the zircon separation process. Martin Robyr and Olivier Reubi (University of Lausanne, Switzerland) and Andreas Karlsson (Swedish Museum of Natural History, Sweden) are thanked for assistance during EPMA, Raman and SEM data acquisition. Great thanks to Daniele Regis for helpful discussions at various stages of this work. We acknowledge NordSIMS for provision of facilities and experimental support and we thank K. Kindén for assistance. NordSIMS is funded by the Swedish Research Council as a national research infrastructure (Dnr. 2021-00276). This is NordSIMS publication number 784 and FIERCE contribution number 187. Nadia Malaspina is thanked for her efficient editorial handling of the manuscript. Chiara Groppo and an anonymous reviewer provided constructive comments that helped us to sharpen our discussion.

Appendix A. Supplementary data

Supplementary data to this article can be found online at https://doi.org/10.1016/j.lithos.2025.107951.

References

Ackerson, M.R., Watson, E.B., Tailby, N.D., Spear, F.S., 2017. Experimental investigation into the substitution mechanisms and solubility of Ti in garnet. Am. Mineral. 102, 158–172.
Angiboust, S., Glodny, J., 2020. Exhumation of eclogitic ophiolitic nappes in the W. Alps: new age data and implications for crustal wedge dynamics. Lithos 356–357, 105374.
Austrheim, H., Putnis, C.V., Engvik, A.K., Putnis, A., 2008. Zircon coronas around Fe-Ti oxides: a physical reference frame for metamorphic and metasomatic reactions. Contrib. Mineral. Petrol. 156, 517–527.
Ballèvre, M., Camonin, A., Manzotti, P., Poujol, M., 2020. A step towards unraveling the paleogeographic attribution of pre-Mesozoic basement complexes in the Western Alps based on U-Pb geochronology of Permian magmatism. Swiss J. Geosci. 113, 12.
Bartoli, O., Millonig, L.J., Carvalho, B.B., Marschall, H.R., Gerdes, A., 2024. The age of granulite-facies metamorphism in the Ivrea-Verbano Zone (NW Italy) determined through in situ U-Pb dating of garnet. J. Pet. 65, egae083.
Baxter, E.F., Caddick, M.J., Dragovic, B., 2017. Garnet: a rock forming mineral petrochronometer. Rev. Mineral. Geochem. 83, 469–533.
Beranoaguirre, A., Vasiliev, I., Gerdes, A., 2022. In situ LA-ICPMS U–Pb dating of sulfates: applicability of carbonate reference materials as matrix-matched standards. Geochronology 4, 601–616.
Bingen, B., Austrheim, H., Whitehouse, M., 2001. Ilmenite as a source for zirconium during high-grade metamorphism? Textural evidence from the Caledonides of Western Norway and implications for zircon geochronology. J. Pet. 42, 355–375.
Bonnet, G., Chopin, C., Locatelli, M., Kylander-Clark, A.R.C., Hacker, B.R., 2022. Protracted subduction of the European hyperextended margin revealed by rutile U-Pb geochronology across the Dora-Maira Massif (Western Alps). Tectonics 41, e2021TC007170.
Bosse, V., Villa, I.M., 2019. Petrochronology and hygrochronology of tectonometamorphic events. Gondwana Res. 71, 76–90.
Bussy, F., Cadoppi, P., 1996. U-Pb dating of granitoids from the Dora-Maira massif (Western Italian Alps). Schweiz. Mineral. Petrogr. Mitt. 76, 217–233.
Cherniak, D.J., 2000. Pb diffusion in rutile. Contrib. Mineral. Petrol. 139, 198–207.
Chopin, C., 1984. Coesite and pure pyrope in high-grade blueschists of the Western Alps: a first record and some consequences. Contrib. Mineral. Petrol. 86, 107–118.
Clark, C., Taylor, R.J.M., Roberts, M.P., Harley, S.L., 2024. Modification of the isotopic and geochemical compositions of accessory minerals controlled by microstructural setting. J. Metamorph. Geol. 42, 957–978.
Dahl, P.S., 1997. A crystal-chemical basis for Pb retention and fission-track annealing systematics in U-bearing minerals, with implications for geochronology. Earth Planet. Sci. Lett. 150, 277–290.
Decarlis, A., Manatschal, G., Haupert, I., Masini, E., 2015. The tectono-stratigraphic evolution of distal, hyper-extended magma-poor conjugate rifted margins: examples from the Alpine Tethys and Newfoundland-Iberia. Mar. Pet. Geol. 68, 54–72.
Dickinson, W.R., Gehrels, G.E., 2009. Use of U-Pb ages of detrital zircons to infer maximum depositional ages of strata: a test against a Colorado Plateau Mesozoic database. Earth Planet. Sci. Lett. 288, 115–125.
Dodson, M.H., 1973. Closure temperature in cooling geochronological and petrological systems. Contrib. Mineral. Petrol. 40, 259–274.
Duchêne, S., Blichert-Toft, J., Luais, B., Tèlouk, P., Lardeaux, J.-M., Albarède, F., 1997. The Lu-Hf dating of garnets and the ages of the Alpine high-pressure metamorphism. Nature 387, 586–589.
Ewing, T.A., Rubatto, D., Lemke, K., Hermann, J., 2023. Timescales and mechanisms of felsic lower continental crust formation: insights from U-Pb geochronology of detrital zircon (Malenco Unit, eastern Central Alps). Lithos 456–457, 107286.
Ferrando, S., Frezzotti, M.L., Petrelli, M., Compagnoni, R., 2009. Metasomatism of continental crust during subduction: the UHP whiteschists from the Southern Dora-Maira Massif (Italian Western Alps). J. Metamorph. Geol. 27, 739–756.
Garber, J.M., Smye, A.J., Feineman, M.D., Kylander-Clark, A.R., Matthews, S., 2020. Decoupling of zircon U-Pb and trace-element systematics driven by U diffusion in eclogite-facies zircon (Monviso meta-ophiolite, W. Alps). Contrib. Mineral. Petrol. 175, 55.
Gerdes, A., Zeh, A., 2006. Combined U–Pb and Hf isotope LA- (MC-) ICP-MS analyses of detrital zircons: comparison with SHRIMP and new constraints for the provenance and age of an Armorican metasediment in Central Germany. Earth Planet. Sci. Lett. 249, 47–61.
Gerdes, A., Zeh, A., 2009. Zircon formation versus zircon alteration—new insights from combined U–Pb and Lu–Hf in situ LA-ICP-MS analyses, and consequences for the interpretation of Archean zircon from the Central Zone of the Limpopo Belt. Chem. Geol. 261, 230–243.
Gilotti, J.A., McClelland, W.C., Schorn, S., Compagnoni, R., Coble, M.A., 2023. Provenance, protolith and metamorphic ages of jadeite-bearing orthogneiss and host paragneiss at Tavagnasco, the Sesia Zone, lower Aosta Valley, Italy. Eur. J. Mineral. 35, 645–658.
Grand'Homme, A., Janots, E., Seydoux-Guillaume, A.M., Guillaume, D., Bosse, V., Magnin, V., 2016. Partial resetting of the U-Th-Pb systems in experimentally altered monazite: Nanoscale evidence of incomplete replacement. Geology 44, 431–434.

Herwartz, D., Nagel, T.J., Münker, C., Scherer, E.E., Froitzheim, N., 2011. Tracing two orogenic cycles in one eclogite sample by Lu-Hf garnet chronometry. Nat. Geosci. 4, 178–183.
Holland, T.J.B., Powell, R., 1998. An internally consistent thermodynamic data set for phases of petrological interest. J. Metamorph. Geol. 16, 309–343.
Horstwood, M.S.A., Košler, J., Gehrels, G., Jackson, S.E., McLean, N.M., Paton, C., Pearson, N.J., Sircombe, K., Sylvester, P., Vermeesch, P., Bowring, J.F., Condon, D.J., Schoene, B., 2016. Community-derived standards for LA-ICP-MS U–(Th-)Pb geochronology – uncertainty propagation, age interpretation and data reporting. Geostand. Geoanal. Res. 40, 311–332.
Jochum, K.P., Weis, U., Stoll, B., Kuzmin, D., Yang, Q., Raczek, I., Jacob, D.E., Stracke, A., Birbaum, K., Frick, D.A., Günther, D., Enzweiler, J., 2011. Determination of reference values for NIST SRM 610-617 glasses following ISO guidelines. Geostand. Geoanal. Res. 35, 397–429.
Kohn, M.J., Corrie, S.L., Markley, C., 2015. The fall and rise of metamorphic zircon. Am. Mineral. 100, 897–908.
Kooijman, E., Mezger, K., Berndt, J., 2010. Constraints on the U-Pb systematics of metamorphic rutile from in situ LA-IPC-MS analysis. Earth Planet. Sci. Lett. 293, 321–330.
Lapen, T.J., Johnson, C.M., Baumgartner, L.P., Dal Piaz, G.V., Skora, S., Beard, L., 2007. Coupling of oceanic and continental crust during Eocene eclogite-facies metamorphism: evidence from the Monte Rosa nappe, western Alps. Contrib. Mineral. Petrol. 153, 139–157.
Ludwig, K.R., 2003. Isoplot/EX, version 3, A geo-chronological toolkit for Microsoft Excel: Berkeley Geochronology Center Special Publication, 4.
Ludwig, K.R., 2008. User's Manual for Isoplot 3.60, A Geochronological Toolkit for Microsoft Excel. 4. Berkeley Geochronological Center Special Publication.
Luvizotto, G.L., Zack, T., Meyer, H.P., Ludwig, T., Triebold, S., Kronz, A., Münker, C., Stockli, D.F., Prowatke, S., Klemme, S., Jacob, D.E., von Eynatten, H., 2009. Rutile crystals as potential trace element and isotope mineral standards for microanalysis. Chem. Geol. 261, 346–369.
Manzotti, P., Ballèvre, M., 2024. Continental subduction in the Alps: From field data to kinematic models. Chapter 5, v.2. In: "Geodynamics of the Alps", Eds: Rosenberg C, Bellahsen N, Sciences – Dynamics of the continental lithosphere. Wiley, pp. 255–313. https://doi.org/10.1002/9781394299539.ch5. ISBN: 9781789451160.
Manzotti, P., Ballèvre, M., Zucali, M., Robyr, M., Engi, M., 2014. The tectonometamorphic evolution of the Sesia–Dent Blanche nappes (internal Western Alps): review and synthesis. Swiss J. Geosci. 107, 309–336.
Manzotti, P., Poujol, M., Ballèvre, M., 2015. Detrital zircon geochronology in blueschist-facies meta-conglomerates from the Western Alps: implications for the late Carboniferous to early Permian palaeogeography. Int. J. Earth Sci. 104, 703–731.
Manzotti, P., Ballèvre, M., Poujol, M., 2016. Detrital zircon geochronology in the Dora-Maira and Zone Houillère: a record of sediment travel paths in the Carboniferous. Terra Nova 28, 279–288.
Manzotti, P., Bosse, V., Pitra, P., Robyr, M., Schiavi, F., Ballèvre, M., 2018. Exhumation rates in the Gran Paradiso Massif (Western Alps) constrained by in situ U-Th-Pb dating of accessory phases (monazite, allanite and xenotime). Contrib. Mineral. Petrol. 173, 24.
Manzotti, P., Schiavi, F., Nosenzo, F., Pitra, P., Ballèvre, M., 2022. A journey towards the forbidden zone: a new, cold, UHP unit in the Dora-Maira Massif (Western Alps). Contrib. Mineral. Petrol. 177, 59.
Manzotti, P., Regis, D., Petts, D.C., Graziani, R., Polivchuk, M., 2024. Formation of multistage garnet grains by fragmentation and overgrowth constrained by microchemical and microstructural mapping. J. Metamorph. Geol. 42, 471–496.
McClelland, W.C., Lapen, T.J., 2013. Linking time to the pressure-temperature path or ultrahigh-pressure rocks. Elements 9, 273–279.
Mezger, K., 1989. U-Pb systematics of garnet: dating the growth of garnet in the late Archean Pikwitonei granulite domain at Cauchon and Natawahunan Lakes, Manitoba, Canada. Contrib. Mineral. Petrol. 101, 136–148.
Michard, A., Schmid, S.M., Lahfid, A., Ballèvre, M., Manzotti, P., Chopin, C., Iaccarino, S., Dana, D., 2022. The Maira-Sampeyre and Val Grana Allochthons (South Western Alps): review and new data on the tectonometamorphic evolution of the Briançonnais distal margin. Swiss J. Geosci. 115, 19.
Millonig, L.J., Albert, A., Gerdes, A., Avigad, D., Dietsch, C., 2020. Exploring laser ablation U-Pb dating of regional metamorphic garnet – the Straits Schist, Connecticut, USA. Earth Planet. Sci. Lett. 552, 116589.
Moore, J., Beinlich, A., Porter, J.K., Talavera, C., Berndt, J., Piazolo, S., Austrheim, H., Putnis, A., 2020. Microstructurally controlled trace element (Zr, U–Pb) concentrations in metamorphic rutile: An example from the amphibolites of the Bergen Arcs. J. Metamorph. Geol. 38, 103–127.
Nemchin, A.A., Horstwood, M.S.A., Whitehouse, M.J., 2013. High-spatial-resolution geochronology. Elements 9, 31–37.
Nosenzo, F., Manzotti, P., Poujol, M., Ballèvre, M., Langlade, J., 2022. A window into an older orogenic cycle: P-T conditions and timing of the pre-Alpine history of the Dora-Maira Massif (Western Alps). J. Metamorph. Geol. 40, 789–821.
Nosenzo, F., Manzotti, P., Robyr, M., 2023. H_2O budget and metamorphic re-equilibration in polycyclic rocks as recorded by garnet textures and chemistry. Lithos 452, 107230.
Nosenzo, F., Manzotti, P., Krona, M., Ballèvre, M., Poujol, M., 2024. Tectonic architecture of the northern Dora-Maira Massif (Western Alps, Italy): field and geochronological data. Swiss J. Geosci. 117, 6.
Powell, R., Holland, T., 2010. Using equilibrium thermodynamics to understand metamorphism and metamorphic rocks. Elements 6, 309–314.
Rasband, W., 1997. ImageJ. In: U.S. National Institutes of Health. U.S. National Institutes of Health. http://imageJ.nih.gov.
Rubatto, D., Angiboust, S., 2015. Oxygen isotope record of oceanic and high-pressure metasomatism: a P-T–time–fluid path for the Monviso eclogites (Italy). Contrib. Mineral. Petrol. 170, 44.
Rubatto, D., Hermann, J., 2001. Exhumation as fast as subduction? Geology 29, 3–6.
Rubatto, D., Hermann, J., 2003. Zircon formation during fluid circulation in eclogites (Monviso, Western Alps): implications for Zr and Hf budget in subduction zones. Geochim. Cosmochim. Acta 67, 2173–2187.
Scaillet, S., 1996. Excess ^{40}Ar transport scale and mechanism in high-pressure phengites: a case study from an eclogitized metabasite of the Dora-Maira nappe, western Alps. Geochim. Cosmochim. Acta 60, 1075–1090.
Scaillet, S., Féraud, G., Ballèvre, M., Amouric, M., 1992. Mg/Fe and [(Mg,Fe)Si-Al_2] compositional control on argon behaviour in high-pressure white micas: A ^{40}Ar/^{39}Ar continuous laser-probe study from the Dora-Maira nappe on the internal western Alps, Italy. Geochim. Cosmochim. Acta 56, 2851–2872.
Schaltegger, U., Schmitt, A.K., Horstwood, M.S.A., 2015. U–Th–Pb zircon geochronology by ID-TIMS, SIMS, and laser ablation ICP-MS: recipes, interpretations, and opportunities. Chem. Geol. 402, 89–110.
Schmitt, A.K., Zack, T., 2012. High-sensitivity U-Pb rutile dating by secondary ion mass spectrometry (SIMS) with an O_2^- primary beam. Chem. Geol. 332-333, 65–73.
Shu, Q., Beranoaguirre, A., Albert, R., Millonig, L.J., Walters, J.B., Marschall, H.R., Gerdes, A., Hoefer, H.E., Hezel, D., Brey, G.P., 2024. Multi-stage ultrahigh temperature metamorphism in the lower crust of the Kaapvaal craton recorded by U-Pb ages of garnet. Contrib. Mineral. Petrol. 179, 49.
Sláma, J., Košler, J., Pedersen, R.B., 2007. Behaviour of zircon in high-grade metamorphic rocks: evidence from Hf isotopes, trace elements and textural studies. Contrib. Mineral. Petrol. 154, 335–356.
Söderlund, U., Patchett, P.J., Vervoort, J.D., Isachsen, C.E., 2004. The ^{176}Lu decay constant determined by Lu–Hf and U–Pb isotope systematics of Precambrian mafic intrusions. Earth Planet. Sci. Lett. 219, 311–324.
Stacey, J.S., Kramers, J.D., 1975. Approximation of terrestrial lead isotope evolution by a two-stage model. Earth Planet. Sci. Lett. 26, 207–221.
Teipel, U., Eichhorn, R., Loth, G., Rohrmüller, J., Höll, R., Kennedy, A., 2004. U-Pb SHRIMP and Nd isotopic data from the western Bohemian Massif (Bayerischer Wald, Germany): Implications for Upper Vendian and lower Ordovician magmatism. Int. J. Earth Sci. 93, 782–801.
Tera, F., Wasserburg, G.J., 1972. U-Th-Pb systematics in three Apollo 14 basalts and the problem of initial Pb in lunar rocks. Earth Planet. Sci. Lett. 14, 281–304.
Thompson, A.B., Connolly, J.A.D., 1990. Metamorphic fluids and anomalous porosities in the lower crust. Tectonophysics 182, 47–55.
Vaggelli, G., Borghi, A., Cossio, R., Fedi, M., Giuntini, L., Lombardo, B., Marino, A., Massi, M., Olmi, F., Petrelli, M., 2006. Micro-PIXE analysis of monazite from the Dora Maira Massif. Western Italian Alps. Microchim. Acta 155, 305–311.
Verberne, R., van Schrojenstein Lantman, H.W., Reddy, S.M., Alvaro, M., Wallis, D., Fougerouse, D., Langone, A., Saxey, D.W., Rickard, W.D.A., 2022. Trace-element heterogeneity in rutile linked to dislocation structures: implications for Zr-in-rutile geothermometry. J. Metamorph. Geol. 41, 3–24.
Vermeesch, P., 2012. On the visualisation of detrital age distributions. Chem. Geol. 312–313, 190–194.
Vermeesch, P., 2018. IsoplotR: a free and open toolbox for geochronology. Geosci. Front. 9, 1479–1493.
Vho, A., Rubatto, D., Lanari, P., Regis, D., 2020. The evolution of the Sesia Zone (Western Alps) from Carboniferous to cretaceous: insights from zircon and allanite geochronooogy. Swiss J. Geosci. 113, 24.
Villa, I.M., 1998. Isotopic closure. Terra Nova 10, 42–47.
Whitehouse, M.J., Kamber, B.S., Moorbath, S., 1999. Age-significance of U-Th-Pb zircon data from early Archean rocks of West Greenland: reassessment based on combined ion-microprobe and imaging studies. Chem. Geol. 160, 210–224.
Wigand, M., Schmitt, A.K., Trumbull, R.B., Villa, I.M., Emmermann, R., 2004. Short-lived magmatic activity in an anorogenic subvolcanic complex: ^{40}Ar/^{39}Ar and ion microprobe U–Pb zircon dating of the Erongo, Damaraland, Namibia. J. Volcanol. Geotherm. Res. 130, 285–305.
Williams, M.L., Jercinovic, M.J., Harlov, D.E., Budzyn, B., Hetherington, C.J., 2011. Resetting monazite ages during fluid-related alteration. Chem. Geol. 283, 218–225.
Zack, T., Kooijman, E., 2017. Petrology and geochronology of rutile. Rev. Mineral. Geochem. 83, 443–467.
Zack, T., Moraes, R., Kronz, A., 2004. Temperature dependence of Zr in rutile: Empirical calibration of a rutile thermometer. Contrib. Mineral. Petrol. 148, 471–488.